GEORG-AUGUST-UNIVERSITÄT
GÖTTINGEN

Fakultät für
Physik

Master's Thesis

Untersuchung der Sensitivität des ATLAS-Detektors für den geboosteten $HH \to WW\tau\tau$ Kanal

ATLAS sensitivity studies for $HH \to WW\tau\tau$ in the boosted topology

prepared by

Nils Gillwald

from Göttingen

at the II. Physikalisches Institut

Thesis number:	II.Physik-UniGö-MSc-2018/05
Thesis period:	28th May 2018 until 30th October 2018
First referee:	Prof. Dr. Stan Lai
Second referee:	Priv.Doz. Dr. Jörn Große-Knetter

Abstract

In this thesis, an estimation of the expected sensitivity of the ATLAS experiment to the $HH \to WW\tau\tau$ channel in $150\,\text{fb}^{-1}$ of data is given. This approximately corresponds to the data set collected by the ATLAS experiment in the years from 2015 to 2018 at a centre-of-mass energy of $\sqrt{s} = 13\,\text{TeV}$. The HH process is assumed to be produced via a heavy CP-even scalar resonance X with a mass of $m_X = 2\,\text{TeV}$, and the production cross section is assumed to be $\sigma_{pp\to X\to HH} = 10\,\text{fb}$. As the resulting topology is boosted, large-R jets and Di-Tau jets are used in order to properly reconstruct the event. An optimization of the event selection is performed, and an assumption on the systematic uncertainties relevant to the analysis is given to assess their impact on the sensitivity.

As no significant deviation of the number of signal events over the background-only hypothesis is expected, the predicted upper limits are given at the 95% confidence level to the cross section times branching ratio of the channel. The expected upper limit is found to be $\sigma_{pp\to X\to HH} = 155^{+69}_{-43}\,\text{fb}$.

Contents

1. Introduction

By the end of the 20$^{\text{th}}$ century, the Standard Model (SM) of particle physics was established. Having its earliest roots in the discovery of the electron by J. J. Thompson in 1897 [1, 2], it combines the electroweak (EW) theory of electromagnetic and weak interactions between leptons and quarks proposed by Glashow, Salam and Weinberg in the 1960s [3–5] with quantum chromodynamics (QCD) [6–9], which describes the strong interaction between quarks and gluons. United, the SM provides a concise theory of three of the four fundamental interactions. It is able to describe interactions between fundamental particles on quantum level in a precise manner due to its perturbative nature at sufficiently high energies and its renormalisability [10–13].

The SM has been tested in various measurements in the past and present, at the Large Electron Positron Collider (LEP) [14], TEVATRON (e.g. [15, 16]) or, more recently and still ongoing, the Large Hadron Collider (LHC). These tests have provided clear evidence that the SM is a successful effective description of EW and strong interactions up to present energies.

A key part of the SM is the Higgs mechanism which causes electroweak symmetry breaking (EWSB). This mechanism, proposed by Brout, Englert, Higgs, Guralnik, Hagen and Kibble [17–19] in the 1960s is an approach for generating masses of the weak vector bosons while preserving the local gauge invariance, renormalisability, and unitarity of the EW theory. Also, the mechanism gives rise to an additional scalar boson known as the Higgs boson, H. The last piece of the SM was set with the discovery of such a scalar boson in 2012 by the ATLAS and CMS collaborations at the LHC [20, 21].

Despite its success in describing EW and strong interactions, the SM is not a complete description of all phenomena which are observed in nature. As a consequence, there are various extensions to the SM being discussed and searched for, including e.g. supersymmetric models (SUSY) or models containing two Higgs doublets (2HDM). However, for the time being it is unknown which model could be a successful addition to the SM.

The topic of this thesis is the investigation of a possible extended Higgs sector. The ATLAS sensitivity to the boosted $HH \rightarrow WW\tau\tau$ channel will be estimated for the single lepton decay channel with the Higgs boson pair originating from a heavy CP-even scalar

resonance, X, modeled with a 2HDM. Monte Carlo simulated events with a resonant mass of $m_X = 2\,\text{TeV}$ are used for this purpose. An integrated luminosity of $\int \mathcal{L} dt = 150\,\text{fb}^{-1}$ is assumed, which is approximately the amount of data taken by the ATLAS experiment at the end of 2018. This analysis might add sensitivity to HH events in addition to the ongoing analyses (e.g. [22–25]).

A more profound discussion of the SM and its interactions is given in Section 2.1, followed by an overview over EWSB and the Higgs boson in Section 2.2. Theories beyond the SM and 2HDM models are described in Section 2.3. Chapter 3 describes the experimental setting of the analysis: The LHC and the ATLAS experiment are described in Section 3.1 and 3.2, and an overview on Monte Carlo generators for event simulation is presented in Section 3.3. Also, an introduction to jet reconstruction in the boosted topology is given in Section 3.4 and 3.5. The analysis strategy is presented in Chapter 4, including a discussion of the event topology, the event selection and the optimization of the event selection based on maximizing the significance. Chapter 5 discusses the statistical interpretation of the analysis, where upper limits on the cross section times branching ratio are set. Chapter 6 concludes the analysis and discusses possible improvements on the analysis.

2. Theoretical Concepts

2.1. The SM particle content and its fundamental interactions

The SM is a well-tested and highly successful effective theory to describe interactions between (fundamental) particles on quantum level. It is based on the $SU(3)_C \times SU(2)_L \times U(1)_Y$ gauge symmetry group of QCD [6–9], $SU(3)_C$, describing the strong force, and the EW sector [3–5], $SU(2)_L \times U(1)_Y$. The conserved quantum number of QCD is the colour C, while the conserved quantum number for the EW sector is the hypercharge Y, with

$$Y = 2(Q - I_3)\,, \tag{2.1}$$

where Q is the electric charge and I_3 is the third component of weak isospin. Gravity is not included in the SM. The SM consists of two types of fields: matter fields, which are spin-$\frac{1}{2}$ fermions, and gauge fields, which are spin-1 bosons mediating the interactions between the fermions. An illustration of this particle content can be found in Figure 2.1.

The matter fields ψ are split in three generations of left-handed and right-handed chiral quarks and leptons – fermions – f, where $f_{L,R} = \frac{1}{2}(1 \mp \gamma_5)f$. The left-handed fermions are sorted into weak isospin doublets, where the upper partner has a third weak isospin component of $I_3 = +\frac{1}{2}$ while the lower has one of $I_3 = -\frac{1}{2}$. The right-handed fermions are however sorted in weak isospin singlets, as the weak force couples to the chirality of the particles. With respect to QCD, quarks are sorted in colour triplets while leptons are sorted in colour singlets, as only the quarks are affected by QCD.

The gauge fields are associated to their respective gauge group. In the EW sector, there are the four fields B_μ and $W_\mu^{1,2,3}$. B_μ corresponds to the generator Y of the $U(1)_Y$ group, while the $W_\mu^{1,2,3}$ fields correspond to the generators T^a, $a \in \{1, 2, 3\}$, of the $SU(2)_L$ group. The generators T^a are proportional to the Pauli matrices with a proportionality constant of $\frac{1}{2}$. After EWSB, linear combinations of these fields will form the experimentally observed bosons: the photon γ, the charged $W^\pm$ and the neutral Z boson. In the strong sector, associated to the $SU(3)_C$ group, there is an octet of gluon fields $G_\mu^{1,\ldots,8}$ cor-

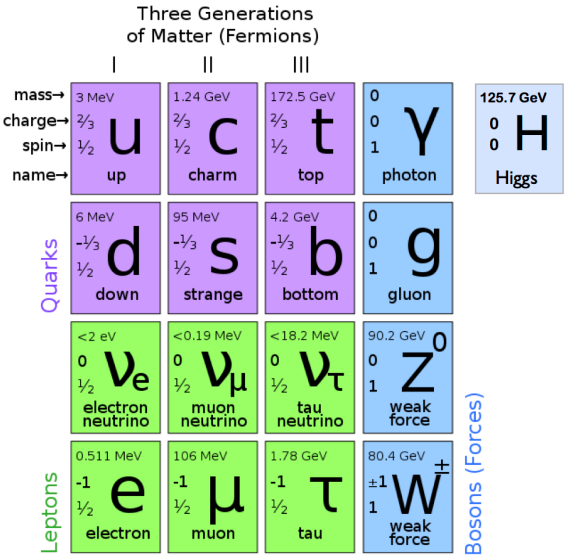

Figure 2.1.: Particle content of the SM. The fermions, split into quarks (purple) and leptons (green), are separated in three generations and sorted by their weak isospin value. To the right are the vector bosons (dark blue) mediating the forces of the SM and the scalar Higgs boson (light blue) originating from EWSB.

responding to the generators of $SU(3)_C$. The latter can be represented by the Gell-Mann matrices, again with a proportionality constant of $\frac{1}{2}$. The gluons are each associated with a different colored state, however, they cannot be distinguished in experiment, as the colour of a particle is not directly observable. From this, the field strength tensors of the fields can be written as

$$\begin{aligned} B^a_{\mu\nu} &= \partial_\mu B_\nu - \partial_\nu B_\mu \,, \\ W^a_{\mu\nu} &= \partial_\mu W^a_\nu - \partial_\nu W^a_\mu + g_2 \epsilon^{abc} W^b_\mu W^c_\nu \,, \\ G^a_{\mu\nu} &= \partial_\mu G^a_\nu - \partial_\nu G^a_\mu + g_s f^{abc} G^b_\mu G^c_\nu \,, \end{aligned} \tag{2.2}$$

where ϵ^{abc} is the fully antisymmetric tensor, f^{abc} denotes the structure constants of QCD, and g_2 and g_s are the coupling constants of the weak and strong force, respectively. The second coupling constant of the EW sector, g_1, does not affect the field strength tensors. As can be seen in Equation 2.2, there are additional terms in the field strength tensors of W^a_μ and G^a_μ, which include quadratic terms in the fields. These account for the non-abelian nature of the group generators, yielding self-interaction terms for the gauge bosons, i.e. triple and quartic gauge boson couplings.

In the SM, a minimal coupling of the gauge bosons to the matter fields is implemented. Explicitly, this is realized by adding terms including the gauge fields to the covariant

derivative $D_\mu\psi$. In this way, also the gauge invariance of the theory under each group transformations is ensured. The complete covariant derivative of the SM with respect to quarks is

$$D_\mu\psi = \left(\partial_\mu - ig_s T_a G_\mu^a - ig_2 T_a W_\mu^a - ig_1 \frac{Y_q}{2} B_\mu\right)\psi\,, \tag{2.3}$$

where T_a are the respective generators of the groups. For the leptons, the covariant derivate is essentially the same as for quarks, only with $g_s = 0$ as they do not interact via the strong force. The SM Lagrangian reads

$$\begin{aligned}\mathcal{L} = -\frac{1}{4}\left(G_{\mu\nu}^a G_a^{\mu\nu} - W_{\mu\nu}^a W_a^{\mu\nu} - B_{\mu\nu}B^{\mu\nu}\right) \\ + \bar{\psi}_L^f i D_\mu \gamma^\mu \psi_L^f + \bar{\psi}_R^f i D_\mu \gamma^\mu \psi_R^f\,,\end{aligned} \tag{2.4}$$

where the first row describes the kinematic terms of the gauge bosons and the second row describes the kinematic terms of the fermions as well as their interactions with the gauge bosons. γ^μ are the Dirac matrices, and $\psi_{L,R}^f$ are the left-handed fermion doublets and right-handed fermion singlets of the EW interaction, and D_μ is the covariant derivative as defined in Equation 2.3.

While the strong and EW forces can be described very well using the SM Lagrangian in the Lagrangian formalism, the described fields to this point remain massless. However, only the photon and gluon are observed to have no mass, while the W and Z bosons as well as the fermions are observed to have non-zero masses [26–28]. A naive estimate to include the mass terms in the SM Lagrangian is to simply add terms of the type

$$\frac{1}{2}m_V V_\mu V^\mu \quad \text{or} \quad \frac{1}{2}m_f \bar{\psi}_f \psi_f = \frac{1}{2}m_f\left(\bar{\psi}_R\psi_L + \bar{\psi}_L\psi_R\right) \tag{2.5}$$

for the gauge bosons V and fermions f, respectively, where m denotes the mass of the respective particle. Such terms will however break the gauge invariance of the Lagrangian under $SU(2)_L \times U(1)_Y$ transformations. Thus, the EW symmetry of the Lagrangian must be broken in order to provide mass terms for the particles. The Brout-Englert-Higgs-Guralnik-Hagen-Kibble (BEH) mechanism provides such a way to introduce mass terms for all SM particles without violating the $SU(2)_L \times U(1)_Y$ gauge invariance. It is described in the following section.

2.2. EWSB and the Higgs Boson

2.2.1. EWSB in the SM[1]

The SM is a non-abelian gauge theory which uses gauge bosons to mediate the fundamental forces. These gauge bosons are experimentally found to be massive [26–28], but the simple insertion of mass terms into the SM Lagrangian would break the $SU(3)_C \times SU(2)_L \times U(1)_Y$ symmetry. Thus, there needs to be a mechanism which provides masses to the weak gauge bosons while preserving the local gauge symmetry. To accomplish this goal, at least three degrees of freedom (DOF) are needed in order to allow the gauge bosons to be vector particles. With the BEH mechanism [17–19], such a mechanism was proposed in the 1960s.
The model contains a complex $SU(2)$ weak isospin doublet of scalar fields ϕ

$$\Phi = \begin{pmatrix} \phi^+ \\ \phi^0 \end{pmatrix} = \frac{1}{\sqrt{2}} \begin{pmatrix} \phi_1 + i\phi_2 \\ \phi_3 + i\phi_4 \end{pmatrix}, \tag{2.6}$$

which has a hypercharge of $Y = 1$. The upper field is charged, such that ϕ^+ and $(\phi^+)^* = \phi^-$ provide the longitudinal degrees of freedom to the $W^\pm$ bosons, while the other is neutral such that it provides these for the Z^0 boson. The locally gauge invariant Lagrangian for this so-called Higgs doublet is

$$\mathcal{L}_H = (D_\mu \Phi)^\dagger (D^\mu \Phi) - \mu^2 \Phi^\dagger \Phi - \lambda \left(\Phi^\dagger \Phi\right)^2, \tag{2.7}$$

where the first term describes the locally gauge invariant kinematics of the doublet and the second and third terms describe the Higgs potential. D_μ is the covariant derivative

$$D_\mu = \partial_\mu + i\frac{g_2}{2}\tau_a W_\mu^a + ig_1\frac{Y}{2}B_\mu, \tag{2.8}$$

which is introduced to ensure local gauge invariance of the $SU(3)_C \times SU(2)_L \times U(1)_Y$ symmetry. For $\lambda > 0$ and $\mu^2 < 0$, a sketch of the Higgs potential is shown in Figure 2.2. Using these conditions, the Higgs potential has an infinite set of degenerate minima for which

$$\phi^\dagger \phi = \frac{1}{2}\sum_{k=1}^{4} \phi_k^2 = \frac{v^2}{2} = -\frac{\mu^2}{2\lambda} \tag{2.9}$$

[1] This section follows the descriptions given in [29, 30].

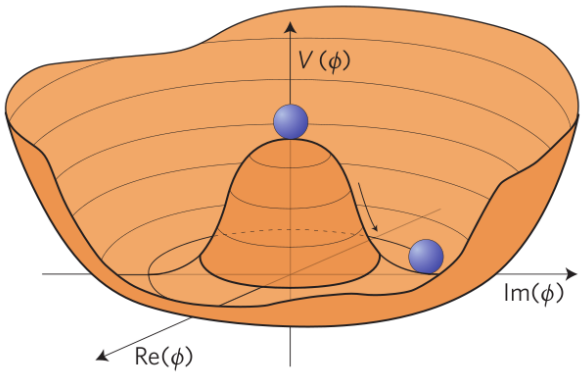

Figure 2.2.: sketch of the Higgs potential for $\lambda > 0$ and $\mu^2 < 0$.

holds. In order to not break the symmetry of quantum electrodynamics (QED) described by the $U(1)_{\mathbf{QED}}$ group, i.e. to keep the photon massless, the minimum of the Higgs potential must be chosen to be in the direction of the neutral scalar field ϕ^0, yielding a non-zero vacuum expectation value (VEV) for the latter

$$\langle \Phi \rangle_0 \equiv \langle 0|\Phi|0\rangle = \begin{pmatrix} 0 \\ \frac{v}{\sqrt{2}} \end{pmatrix} \tag{2.10}$$

where the definition of the VEV can be extracted from Equation 2.9. Expanding the field Φ around the minimum in terms of four fields $\theta_{1,2,3}(x)$ and $H(x)$ at first order yields

$$\Phi(x) = \begin{pmatrix} \theta_2 + i\theta_1 \\ \frac{1}{\sqrt{2}}(v + H) - i\theta_3 \end{pmatrix} = \exp\left(i\theta_a(x)\tau^a(x)/v\right) \begin{pmatrix} 0 \\ \frac{1}{\sqrt{2}}(v + H(x)) \end{pmatrix} \tag{2.11}$$

with the Pauli matrices τ^a, which are by a factor of two the generators of the weak interaction group. Making the gauge transformation

$$\Phi(x) \rightarrow \exp\left(-i\theta_a(x)\tau^a(x)/v\right)\Phi(x) = \frac{1}{\sqrt{2}} \begin{pmatrix} 0 \\ v + H(x) \end{pmatrix} \tag{2.12}$$

yields the Higgs doublet in the unitary gauge. Expanding the kinematic term of the Higgs Lagrangian from Equation 2.7 yields

$$|D_\mu \Phi|^2 = \frac{1}{2}(\partial_\mu H)^2 + \frac{1}{8}g_2^2(v + H)^2|W_\mu^1 + iW_\mu^2|^2 + \frac{1}{8}(v + H)^2|g_2 W_\mu^3 - g_1 B_\mu|^2, \tag{2.13}$$

where g_2 and g_1 are the coupling constants of the $SU(2)_L$ and $U(1)_Y$ symmetry groups, respectively, and W_μ^i and B_μ are the gauge fields before EWSB. The fields of the observed

vector bosons $W^{\pm}$, Z^0 and A can then be defined as

$$W^{\pm} = \frac{1}{\sqrt{2}}\left(W^1_\mu \mp iW^2_\mu\right), \quad Z_\mu = \frac{g_2 W^3_\mu - g_1 B_\mu}{\sqrt{g_2^2 + g_1^2}}, \quad A_\mu = \frac{g_2 W^3_\mu + g_1 B_\mu}{\sqrt{g_2^2 + g_1^2}}, \tag{2.14}$$

where A describes the photon. Applying this definition to Equation 2.13 and searching for quadratic terms in the fields $W^{\pm}$, Z^0 and A yields the mass of each of the fields

$$M_W = \frac{1}{2} v g_2, \quad M_Z = \frac{1}{2} v \sqrt{g_2^2 + g_1^2}, \quad M_A = 0. \tag{2.15}$$

Thus, the photon remains massless while the $W^{\pm}$ and Z^0 bosons receive additional degrees of freedom from the θ_i fields of the Higgs doublet through the gauge transformation to the unitary gauge, so they can have a mass and a longitudinal polarisation.[2]

The masses for the fermions can be generated in a similar way. For this purpose, the same field Φ as before can be used, as well as the isospin doublet $\tilde{\Phi}^* = i\tau_2\Phi^*$. $\tilde{\Phi}$ has a hypercharge of $Y = -1$. For each generation of fermions, the term

$$\mathcal{L}_F = -\lambda_e \bar{L}\Phi e_R - \lambda_d \bar{Q}\Phi d_R - \lambda_u \bar{Q}\tilde{\Phi} u_R + h.c. \tag{2.16}$$

is added to the SM Lagrangian, where $\lambda_{e,d,u}$ are the Yukawa couplings and Q is the electric charge. Repeating the above mechanism for e.g. the electron yields

$$\mathcal{L}_{F,e} = -\frac{1}{\sqrt{2}} \lambda_e (v + H) \bar{e}_L e_R. \tag{2.17}$$

The mass terms of the fermions are those that are quadratic in the fermion field and do not contain any other fields. This gives

$$m_f = \frac{\lambda_f v}{\sqrt{2}}, \tag{2.18}$$

where f is any fermion.

In the above manner, all mass terms needed for the particles in the SM – i.e. the $W^{\pm}$, Z^0 and the fermions – can be generated. The mechanism preserves the EW $SU(2)_L \times U(1)_Y$ local gauge symmetry, although it is spontaneously broken or hidden. At the same time, both the strong colour symmetry from the $SU(3)_C$ group and the electromagnetic $U(1)_{QED}$ symmetry remain unbroken.

[2] Looking at the EWSB mechanism in more detail, these DOF absorbed by the vector bosons first appear as massless so-called Goldstone bosons but are attributed to the vector bosons when applying the unitary gauge.

2.2.2. The Higgs Boson in the SM

The Higgs boson is a CP-even scalar particle [26]. Its mass is defined by the parameters of the Higgs potential in Equation 2.7. Expanding the kinetic part of this Lagrangian and looking at the resulting terms quadratic in the Higgs field, H, yields [29, 30]

$$m_H^2 \;=\; 2\lambda v^2 \;=\; -2\mu^2\,. \tag{2.19}$$

The mass has been measured to be $m_H \;=\; (125.09 \pm 0.21\,(\text{stat}) \pm 0.11\,(\text{syst}))$ GeV by the ATLAS and CMS collaborations [31]. The Higgs boson couples to all massive SM particles either via gauge or Yukawa couplings. Thus, it couples to all particles except neutrinos, the photon and the gluon. The Higgs boson also couples to itself, as it is a massive particle. Expanding the Lagrangian from Equation 2.7 yields trilinear and quartic coupling terms

$$\mathcal{L}_H \;=\; \ldots - \lambda v H^3 - \frac{1}{4}\lambda H^4 \tag{2.20}$$

with couplings both proportional to the parameter λ of the Higgs potential. The corresponding Feynman diagrams are shown in Figure 2.3, where the coupling strengths are marked in red.

2.2.3. Production of Higgs Boson Pairs at the LHC

At the LHC, Higgs bosons can be produced individually (via gluon-gluon fusion (ggF), vector boson fusion (VBF), Higgsstrahlung, associated Higgs top production) or in pairs. Only the latter case is described here.

The most important Feynman diagrams for HH production at the LHC are shown in Figure 2.4a and 2.4b. Looking at SM processes only, Higgs boson pairs can be produced via a fermion loop – dominated by the top quark – (Figure 2.4a) or via Higgs boson self

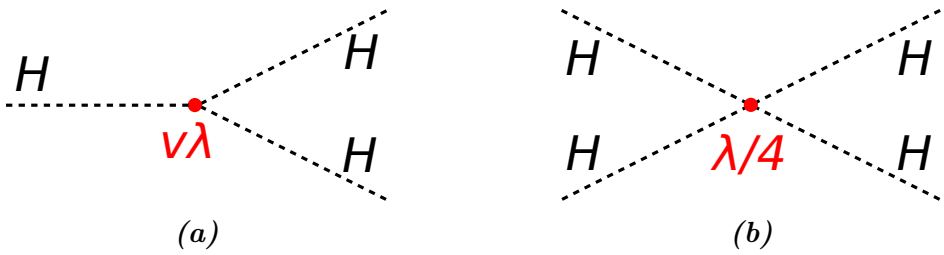

(a) *(b)*

Figure 2.3.: Feynman diagram for the (a) trilinear and (b) quartic Higgs boson self couplings. The vertex and the coupling strength are sketched in red.

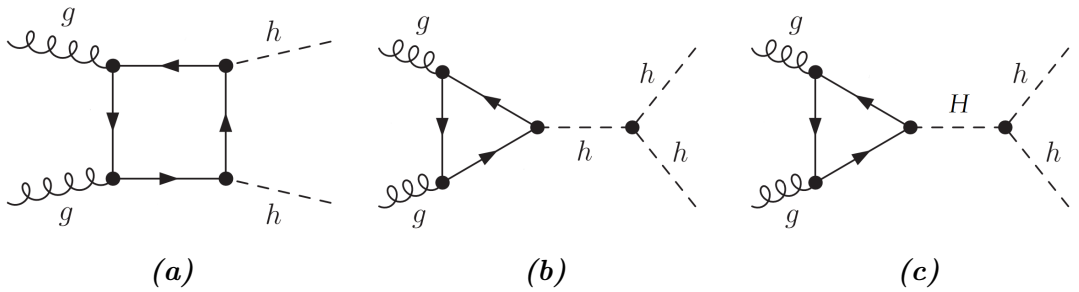

Figure 2.4.: HH production processes at the LHC: (a) production via a quark loop, (b) production via a SM Higgs boson decay, (c) production via a BSM Higgs boson decay.

coupling (Figure 2.4b). The trilinear Higgs vertex of the latter process is of particular interest, as it provides access to a direct measurement of λ and thus the Higgs potential (compare Section 2.2.2). Since the parameter λ can also be accessed via measurements of the Higgs boson mass $m_H = \sqrt{2\lambda}v$ (compare Equation 2.19), these two different measurements of λ can be compared and the SM predictions can be tested.
However, the production of Higgs boson pairs has a low cross section due to the destructive interference of the production via self coupling and via a fermion loop. The most precise theoretical prediction of the HH production cross section via ggF for $m_H = 125.09\,\text{GeV}$ at a centre-of-mass energy of $\sqrt{s} = 13\,\text{TeV}$ at NNLL matched to NNLO including top quark mass effects at NLO is $\sigma_{ggF} = \left(33.49^{+4.3\%}_{-6.0\%}\,(\text{scale}) \pm 2.1\%\,(\text{PDF}) \pm 2.3\%\,(\alpha_S)\right)$ fb [32]. The scale uncertainty comes from the choice of the renormalization scale, the PDF uncertainty is due to the uncertainty of the proton parton density function and the α_s uncertainty is from the uncertainty of the strong coupling constant α_s at the assumed renormalization scale.

In addition to the production via SM processes, Higgs boson pairs can also be produced via beyond SM (BSM) processes. An example process – which is also the process relevant to my master thesis – is shown in Figure 2.4c. There, the Higgs boson pair is produced via a heavy CP-even scalar from a 2HDM. This type of model is discussed in Section 2.3.1. BSM processes such as Higgs pair production via such heavy resonances would change both the measured production cross section and the invariant mass distribution, via a resonant excess in the expected m_{HH} spectrum, found from measurements of HH processes. Thus, in investigating HH final states, both the SM can be probed and a search for new physics can be conducted.

2.2.4. Higgs Boson Decays

As stated previously, the Higgs boson couples to all massive particles in the SM and decays into all SM particles but the top quark, which is heavier than the Higgs boson. The branching ratios ($\mathcal{BR}$) of the dominant Higgs boson decay channels are shown in Table 2.1a.

Because the b quark is the heaviest particle with a mass below half the Higgs boson mass, the Higgs boson most probably decays into a pair of b quarks. The second highest $\mathcal{BR}$ is the decay into an on-shell and an off-shell W boson, followed by the decay into two gluons. The latter is a next to leading order (NLO) process, where the Higgs boson couples to the gluons via a fermion loop.[3] Its detection at hadron colliders is extremely difficult due to the tremendous amount of background processes. The fourth most probable decay is the decay into two τ leptons, followed by the decay into an on-shell and an of-shell Z boson and the NLO decay into two photons.

Decay Mode	$\mathcal{BR}$
$b\bar{b}$	0.581(8)
WW^*	0.215(3)
gg	0.082(5)
$\tau\tau$	0.0626(11)
$c\bar{c}$	0.0288(10)
ZZ^*	0.0264(5)
$\gamma\gamma$	0.00227(5)

(a)

Decay Mode	$\mathcal{BR}$
$b\bar{b}b\bar{b}$	0.338(10)
$b\bar{b}WW^*$	0.250(5)
$b\bar{b}\tau\tau$	0.0727(16)
WW^*WW^*	0.0630(13)
$b\bar{b}ZZ^*$	0.0307(8)
$WW^*\tau\tau$	0.0269(6)
WW^*ZZ^*	0.0114(3)

(b)

Table 2.1.: Branching ratios of (a) the leading Higgs boson decay modes at a Higgs boson mass of $m_H = 125.09\,\text{GeV}$ (b) the leading decay modes of a pair of Higgs bosons at a mass of $m_H = 125.09\,\text{GeV}$ each [32].

In this thesis, the decay of two Higgs bosons into a pair of τ leptons and W bosons is investigated. With a $\mathcal{BR}$ of 0.0269 [32], it is the sixth highest HH decay channel and has never been investigated before. The $\mathcal{BR}$ of the dominant Higgs boson pair decay modes are summarized in Table 2.1b.

Both the τ leptons and the W bosons will decay before reaching the detector, each in two possible ways: leptonically or hadronically. First of all, the W boson could either decay into a τ lepton, muon, or electron and the corresponding neutrino, or into a pair of quarks, $q'\bar{q}$. The τ lepton would first decay into an off-shell W boson and a τ neutrino.

[3] Most probably, the fermion loop will be a top quark loop, as the top quark is the heaviest particle.

The W boson would then decay further, either into a muon or electron and the corresponding neutrino, or into $q'\bar{q}$. This gives rise to multiple possible decay signatures:

- In the fully hadronic channel, all τ leptons and W bosons decay hadronically. This signature has a $\mathcal{BR}$ of 0.2385 with respect to all possible $WW\tau\tau$ decays.[4]
- In the single lepton channel, one τ lepton or W boson decays leptonically, while the others all decay hadronically. This signature has a $\mathcal{BR}$ of 0.4134 which is the highest of the possible channels.
- In the 2-lepton channel, two of the Higgs boson decay products decay leptonically and the other two decay hadronically. Thus, either the W boson or τ lepton side decays fully hadronically while the other side decays fully leptonically, or both sides decay semi-leptonically. This signature has a $\mathcal{BR}$ of 0.2654.
- In the 3-lepton channel, only one Higgs boson decay product decays hadronically, while the others all decay leptonically. This signature has a $\mathcal{BR}$ of 0.0748.
- In the fully leptonic channel, all Higgs boson products decay leptonically. With a $\mathcal{BR}$ of 0.0078, this signature is the least probable one.

Due to time constraints, not all of these signatures can be investigated. This analysis is focused on the single lepton channel, where the lepton comes from the decay of one of the W bosons. The total $\mathcal{BR}$ for this channel is

$$\begin{aligned}\mathcal{BR}&\left(HH \rightarrow W^{\pm}W^{\pm}\tau\tau \rightarrow 2q\ell\nu_{\ell}2\nu_{\tau}4q\right)\\ &= \mathcal{BR}\left(HH \rightarrow W^{\pm}W^{\pm}\tau\tau\right) \times \mathcal{BR}\left(W^{\pm}W^{\pm}\tau\tau \rightarrow 2q\ell\nu_{\ell}2\nu_{\tau}4q\right)\\ &= 6.6 \cdot 10^{-3}\,. \end{aligned} \tag{2.21}$$

The properties of the channel and the used topology will be further discussed in Chapter 4.

2.2.5. The Discovery of the Higgs Boson

The Higgs boson was discovered at the ATLAS and CMS experiments at the LHC at CERN in 2012 [20, 21]. The corresponding plot for the ATLAS experiment is shown in Fig-

[4] All $\mathcal{BR}$ in this list are calculated w.r.t. all possible $WW\tau\tau$ decays. Also, the fact that W bosons might decay into τ leptons which subsequently decay hadronically or leptonically, which can not be observed in the detector as it happens before the particles reach the innermost layer, is accounted for: a W boson decaying hadronically via an intermediate τ lepton is counted as a hadronically decaying W boson, while a W boson decaying leptonically via an intermediate τ lepton is counted as a leptonically decaying W boson.

ure 2.5. The ATLAS collaboration observed a local excess of $5.9\,\sigma$ at an invariant mass of $m_H = 126.5\,\text{GeV}$, while the CMS collaboration observed a local excess of $5\,\sigma$ at an invariant mass of $m_H = 125.5\,\text{GeV}$. The main discovery channels were $H \to \gamma\gamma$ and $H \to ZZ^* \to 4\ell$ ($\ell = e, \mu$), as they provide very clear signatures in the detectors. The latest combined ATLAS and CMS Higgs boson mass measurement yields $m_H = (125.09 \pm 0.21\,(\text{stat}) \pm 0.11\,(\text{syst}))\,\text{GeV}$ [31].

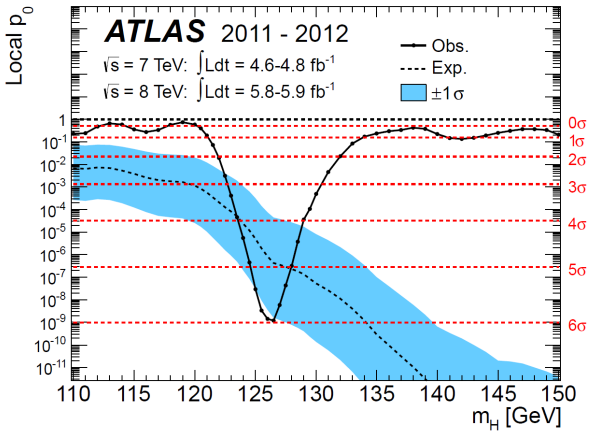

Figure 2.5.: Significances of the observation of a SM Higgs boson like particle by the ATLAS collaboration [20, 21]. The particle with a mass of $m_H = 126.5\,\text{GeV}$ was observed with a local significance of $5.9\,\sigma$.

2.3. Physics Beyond the SM

Present day precision measurements e.g. at the LHC experiments have shown the validity of the SM up to the EW scale [29]. Still, many questions remain unsolved and various theories exist trying to explain these observations.

To begin with, the SM has many free parameters (19) [29].[5] While this is not problematic in itself, it would be preferable to have a theory which predicts most of its parameters rather than one which mostly needs to be fixed by measurements. Also, gravity is not included in the SM because it is not quantisable with current standard procedures due to dimensional reasons.

Trying to explain the formation of the universe, it is still unclear why there is such an imbalance between matter and antimatter during baryogenesis yielding the observed

[5] This ignores (a) six parameters from the neutrino sector, ignoring the existence of neutrino masses and oscillation (which is strictly not a part of the SM) and (b) a possible CP violating phase in QCD, which experimentally is known to be approximately zero.

matter-dominated universe [33]. The issue is known to be caused by CP violation, however, the CP violation originating from the CKM matrix in the EW sector is not sufficient to account for this imbalance and there must be further sources of CP violation.

Observations of the rotational properties of galaxies tell us, that the amount of baryonic matter we observe in these very galaxies is not sufficient to describe their rotational velocity distributions [34], which hints at the existence of so-called dark matter (DM), and observations of distant supernovae hint at an accelerated expansion of our universe [35], being explained by dark energy of which the nature is unknown.

In the Higgs sector, the hierarchy problem occurs [36]: If the SM is correct up to the mass scale of a grand unified theory (GUT) or the Planck scale at $\Lambda_{\mathrm{GUT}} \approx 10^{16}$ or $\Lambda_{\mathrm{P}} \approx 10^{19}\,\mathrm{GeV}$, respectively, the quantum loop corrections to the Higgs boson propagator at $\Lambda_{\mathrm{EW}} \approx 10^{3}\,\mathrm{GeV}$ must cancel with a precision of $\mathcal{O}(10^{-30})$. While this intrinsically causes no problem, it does not seem to be a realistic scenario that all these large corrections of the order of $\Lambda^2_{\mathrm{GUT/P}}$ are fine-tuned to yield a Higgs mass at the EW scale.

Most of the proposed theories that would solve the above problems include additional particles. Most prominently, this includes supersymmetric (SUSY) models. The basic idea of SUSY expansions to the SM, supersymmetric standard models (SSM), is to link each SM particle to a SUSY partner. Except for the spin, where they differ by $\frac{1}{2}$ unit, these partners coincide in all quantum numbers. This means, that all SM fermions have a spin-0 and all SM bosons, be it vector or scalar, have a spin-$\frac{1}{2}$ supersymmetric partner. These partners are referred to as sfermions and bosinos, respectively [37]. The existence of such partners would cancel all loop corrections to the Higgs propagator, solving the hierarchy problem. Also, if the weakest SUSY particle (sparticle) were to be stable, it would make a perfect DM candidate.[6]

As multiplets of different chiralities are not allowed to couple together in the Lagrangian, and as all gauge anomalies must cancel, a second Higgs doublet is needed in these models [39–43]. In consequence, a SUSY model always is a 2HDM model.

Other, not so prominent motivations for the existence of 2HDM arise from axions models [44] or from the fact that 2HDM models are capable of providing a sufficiently high amount of CP violation to explain the baryon asymmetry observed in the universe [45].

[6] This implies the conservation of R-parity, a quantum number which is +1 for all SM particles and -1 for all SSM sparticles [38].

2.3.1. Two Higgs Doublet Models

EWSB in the minimal SSM

The minimal supersymmetric standard model (MSSM) is the minimal possible SUSY expansion of the SM. As discussed in the previous section, it needs two Higgs doublets in order to provide the mass terms for all fundamental particles in the model. Thus, two Higgs doublets with opposite hypercharge are defined

$$\Phi_1 = \begin{pmatrix} \phi_1^0 \\ \phi_1^- \end{pmatrix} \text{ with } Y = -1 \text{ and } \Phi_2 = \begin{pmatrix} \phi_2^+ \\ \phi_2^0 \end{pmatrix} \text{ with } Y = +1\,. \tag{2.22}$$

This results in one VEV for each field, v_1 and v_2, respectively, with the definition

$$v = \sqrt{v_1^2 + v_2^2}\,. \tag{2.23}$$

Also,

$$\tan\beta = \frac{v_2}{v_1} \tag{2.24}$$

is defined, which is an important parameter to the MSSM. As in the EWSB for the SM, the two Higgs doublets are now expanded around their vacuum state

$$\Phi_1 = \frac{1}{\sqrt{2}} \begin{pmatrix} v_1 + h_1 + i\theta_1 \\ \phi_1^- \end{pmatrix} \text{ and } \Phi_2 = \frac{1}{\sqrt{2}} \begin{pmatrix} \phi_2^+ \\ v_2 + h_2 + i\theta_2 \end{pmatrix}, \tag{2.25}$$

where the imaginary terms generate the CP-odd Higgs bosons and the Goldstone bosons and the real terms generate the CP-even Higgs bosons. Conducting a change of basis, the physical particles are obtained via

$$\begin{pmatrix} G^0 \\ A \end{pmatrix} = \begin{pmatrix} \cos\beta & \sin\beta \\ -\sin\beta & \cos\beta \end{pmatrix} \begin{pmatrix} \theta_1 \\ \theta_2 \end{pmatrix}, \begin{pmatrix} G^\pm \\ H^\pm \end{pmatrix} = \begin{pmatrix} \cos\beta & \sin\beta \\ -\sin\beta & \cos\beta \end{pmatrix} \begin{pmatrix} \phi_1^\pm \\ \phi_2^\pm \end{pmatrix} \text{ and}$$
$$\begin{pmatrix} H \\ h \end{pmatrix} = \begin{pmatrix} \cos\alpha & \sin\alpha \\ -\sin\alpha & \cos\alpha \end{pmatrix} \begin{pmatrix} h_1 \\ h_2 \end{pmatrix}, \tag{2.26}$$

where α is the mixing angle of the CP-even Higgs bosons and G^0 and $G^\pm$ are the Goldstone bosons. As visible, the mechanism does not only yield one but five Higgs bosons: two CP-even scalar bosons h and H, of which one is light and one is heavy, one CP-odd scalar boson A and two charged Higgs bosons $H^\pm$. Often, the light CP-even scalar is referred to

as the SM-like Higgs boson, however, in reality it is a mixture of the two CP-even scalars

$$h_{SM} = h \sin(\alpha - \beta) - H \cos(\alpha - \beta) \,. \tag{2.27}$$

From the remaining six parameters – four masses and two mixing angles – only two parameters are free at tree level because of the many constraints of the MSSM. The normal convention is to choose these free parameters to be m_A and $\tan\beta$.
This extension of the Higgs sector gives rise to new signatures or potentially modifies SM detector signatures, giving rise to searches for the additional MSSM Higgs bosons or modified signatures. In particular, the heavy CP-even scalar can decay into two light Higgs bosons h.

Two Higgs Doublet Models

In general, 2HDMs can extend the SM not only in the context of SUSY, but also independently. Normally, such extensions contain scalar mediated flavour changing neutral currents (FCNC), which are strongly constrained by experiment. They also can be CP preserving or violating. The most general scalar version of 2HDMs contains 14 parameters. However, most experimental studies make simplifying assumptions, such as CP conservation in the Higgs sector and the existence of discrete symmetries forcing the elimination of all quartic terms containing one or three Higgs doublets from the potential.

The two Higgs doublets, both carrying a hypercharge of $Y = +1$, can be parametrized as

$$\Phi_k = \begin{pmatrix} \phi_k^+ \\ \phi_k^0 \end{pmatrix} \quad \text{with} \quad Y = +1 \quad \text{and} \quad k = 1, 2 \,. \tag{2.28}$$

Consequently, there exist two VEVs, v_1 and v_2, respectively, one for each of the doublets. They have the same properties as defined in Equation 2.23 and 2.24. As for EWSB in the SM, the fields can be expanded about their minima

$$\Phi_k = \begin{pmatrix} \Phi_k^+ \\ v_k + h_k + i\theta_k \end{pmatrix} . \tag{2.29}$$

This again yields five Higgs bosons and three Goldstone bosons, which provide the longitudinal degrees of freedom for the weak gauge bosons. However, their properties will differ from the ones in the previous sections, as in this example two doublets with $Y = 1$ are used, in contrast to two doublets with $Y = +1$ and -1, respectively. The difference in Y is needed in order to cancel chiral anomalies. The most general potential containing

Model	u_R^i	d_R^i	ℓ_R^i
Type I	Φ_2	Φ_2	Φ_2
Type II	Φ_2	Φ_1	Φ_1
Lepton-specific	Φ_2	Φ_2	Φ_1
Flipped	Φ_2	Φ_1	Φ_2

Table 2.2.: 2HDMs with natural flavour conservation and the couplings of the Higgs doublets to the different types of fermions. The superscript i is a generational index and u_R^i always couples to Φ_2 by convention [48].

the two doublets Φ_1 and Φ_2 with a hypercharge of $Y = +1$ is [46]

$$\begin{aligned} V =& \lambda_1 \left(|\Phi_1|^2 - v_1^2\right)^2 + \lambda_2 \left(|\Phi_2|^2 - v_2^2\right)^2 + \lambda_3 \left(|\Phi_1|^2 - v_1^2 + |\Phi_2|^2 - v_2^2\right)^2 \\ &+ \lambda_4 \left(|\Phi_1|^2 |\Phi_2|^2 - |\Phi_1^\dagger \Phi_2|^2\right) + \lambda_5 \left(\mathrm{Re}\left(\Phi_1^\dagger \Phi_2\right) - v_1 v_2\right)^2 + \lambda_6 \left(\mathrm{Im}\left(\Phi_1^\dagger \Phi_2\right)\right)^2 \end{aligned} \tag{2.30}$$

with only real parameters λ_j. The parameters λ_j as well as their dependence on the masses and angles can be shown to be [47]

$$\begin{aligned} \lambda_1 &= \frac{1}{4\cos^2(\beta)\, v^2} \left(\cos^2(\alpha)\, m_H^2 + \sin^2(\alpha)\, m_h^2\right) - \frac{\sin(2\alpha)}{\sin(2\beta)} \frac{m_H^2 - m_h^2}{4v^2} + \frac{\lambda_5}{4} \left(1 - \frac{\sin^2(\beta)}{\cos^2(\beta)}\right), \\ \lambda_2 &= \frac{1}{4\sin^2(\beta)\, v^2} \left(\sin^2(\alpha)\, m_H^2 + \cos^2(\alpha)\, m_h^2\right) - \frac{\sin(2\alpha)}{\sin(2\beta)} \frac{m_H^2 - m_h^2}{4v^2} + \frac{\lambda_5}{4} \left(1 - \frac{\cos^2(\beta)}{\sin^2(\beta)}\right), \\ \lambda_3 &= \frac{\sin(2\alpha)}{\sin(2\beta)} \frac{m_H^2 - m_h^2}{4v^2} - \frac{\lambda_5}{4}, \quad \lambda_4 = \frac{m_{H^\pm}^2}{v^2} \text{ and } \lambda_6 = \frac{m_A^2}{v^2}. \end{aligned} \tag{2.31}$$

As no experimental or theoretical constraints need to be met, no masses or angles depend on each other. Thus, the model has six free parameters (eleven parameters less five equations). If additionally the 2HDM is symmetric under the transformation $\Phi_1 \to -\Phi_1$, λ_5 vanishes and the model only has five free parameters left. Otherwise, the existence of λ_5 as an additional free parameter is a relict of the fact that $\tan\beta$ is not constrained in 2HDMs.

Up to this day, no FCNC have been observed at tree level. This only leaves the possibility of four general types of 2HDMs: so-called Type I, Type II, lepton-specific and flipped models, compared in Table 2.2. The difference between these models manifests itself in the couplings of the models to the up- and down-type quarks and the leptons, as shown in Table 2.3. In Type I 2HDMs [49, 50], all fermions couple to the same Higgs doublet, which is conventionally chosen to be Φ_2.[7] At $\alpha = \frac{\pi}{2}$, the Type I models are fermiophobic, meaning that the light Higgs boson decouples from the fermions. In Type II 2HDMs

[7] By convention, up-type quarks are always chosen to couple to Φ_2.

Fermion	Boson	Coupling in 2HDM			
		Type I	Type II	Lepton-specific	Flipped
up-type quarks	h	$\cos\alpha/\sin\beta$	$\cos\alpha/\sin\beta$	$\cos\alpha/\sin\beta$	$\cos\alpha/\sin\beta$
	H	$\sin\alpha/\sin\beta$	$\sin\alpha/\sin\beta$	$\sin\alpha/\sin\beta$	$\sin\alpha/\sin\beta$
	A	$\cot\beta$	$\cot\beta$	$\cot\beta$	$\cot\beta$
down-type quarks	h	$\cos\alpha/\sin\beta$	$-\sin\alpha/\cos\beta$	$\cos\alpha/\sin\beta$	$-\sin\alpha/\cos\beta$
	H	$\sin\alpha/\sin\beta$	$\cos\alpha/\cos\beta$	$\sin\alpha/\sin\beta$	$\cos\alpha/\cos\beta$
	A	$-\cot\beta$	$\tan\beta$	$-\cot\beta$	$\tan\beta$
ℓ	h	$\cos\alpha/\sin\beta$	$-\sin\alpha/\cos\beta$	$-\sin\alpha/\cos\beta$	$\cos\alpha/\sin\beta$
	H	$\sin\alpha/\sin\beta$	$\cos\alpha/\cos\beta$	$\cos\alpha/\cos\beta$	$\sin\alpha/\sin\beta$
	A	$-\cot\beta$	$\tan\beta$	$\tan\beta$	$-\cot\beta$

Table 2.3.: Proportionality factors to the Yukawa couplings of the fermions to the neutral Higgs bosons for the different 2HDMs. The coupling of the charged Higgs bosons are the same as the couplings of A [48].

[50, 51], the up-type quarks couple to one Higgs doublet, while down-type quarks and leptons couple to the other. In general, it is assumed in Type I and II models that leptons couple to the same Higgs doublet as the down-type quarks, however, this must not be the case: In the lepton-specific 2HDMs [52, 53], the quarks couple to one Higgs doublet while the leptons couple to the other. In the last possible 2HDM [52, 53], the flipped model, up-type quarks and leptons couple to the same Higgs doublet, while down-type quarks couple to the other.

Type II 2HDMs are the most studied 2HDMs, as the MSSM is a highly constrained Type II 2HDM, whereas the flipped model is the least studied. A more detailed description which also contains FCNC 2HDMs can be found in [48].

3. The Experimental Setting: the LHC and the ATLAS Experiment

3.1. The Large Hadron Collider

The idea of building a hadron collider instead of a lepton collider already came up in the late 1970s. A more detailed plan for the design of such a hadron collider at CERN was specified in 1984 [54]. The LHC [55] was approved in 1996 [54] and started operating in 2008. It is an underground synchrotron particle accelerator with a circumference of 27 km, designed to accelerate proton or heavy ion beams. In this thesis, only processes using proton beams will be discussed. The design beam energy of the LHC is 7 TeV, resulting in a design collision energy $\sqrt{s}$ of 14 TeV. In contrast to a lepton collider, the limiting factor to the beam energy is not the synchrotron radiation but the strength of the magnetic dipoles used for bending the protons on the circular path. In the LHC tunnel, there are 1232 superconducting dipole magnets, each providing a magnetic field of 8.33 T strength. The magnets are made from NbTi and have an operating temperature below 2 K. In addition to the dipole magnets, quadrupole magnets and magnets of higher order are used to focus the beam and apply higher order scale corrections to the beam path. The protons are accelerated using 16 high frequency radio cavities with a gradient of 2 MV/m. Due to the circular structure, each accelerating unit is used multiple times in the acceleration process. As the LHC is designed to accelerate protons or ions of the same charge, two beam pipes are needed as two magnetic fields of opposite polarity are required in order to keep all particles on their paths. The design instantaneous luminosity of the LHC is $\mathcal{L}_{\text{Design}} = 10^{34}\,\text{cm}^{-2}\text{s}^{-1}$.[1] During Run 2 of the LHC between 2015 and 2018, the LHC operated at $\sqrt{s} = 13\,\text{TeV}$, while a peak luminosity of $2.14 \cdot 10^{34}\,\text{cm}^{-2}\text{s}^{-1}$ was reached by the ATLAS experiment [56].

A sketch of the CERN accelerator complex including the LHC and its accelerator chain is shown in Figure 3.1. Protons are accelerated using this chain of accelerators as follows:

[1] In the previous chapter, $\mathcal{L}$ was used for Lagrangians. In the following, it will always represent luminosities, unless explicitly stated otherwise.

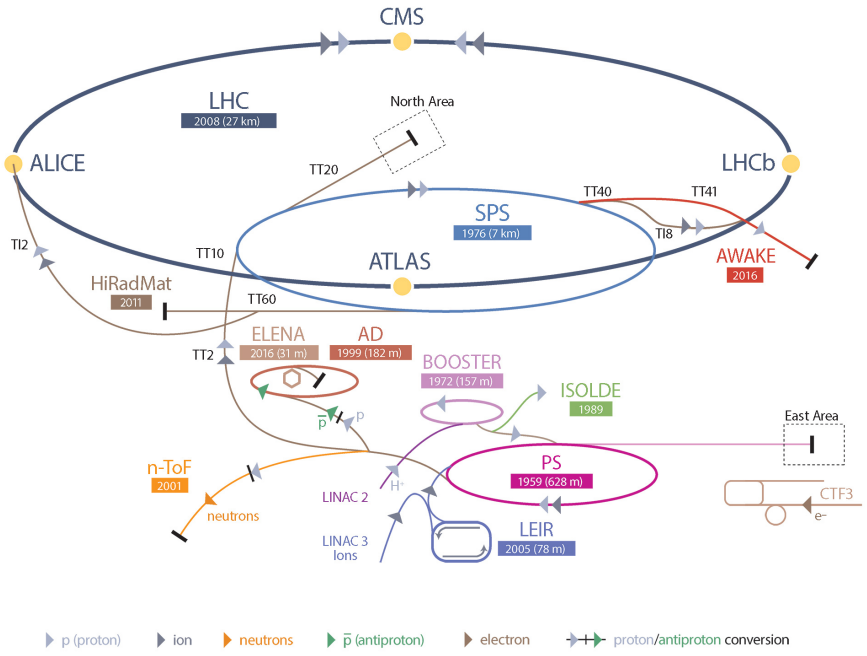

Figure 3.1.: Schematic view of the CERN accelerator complex. © 2008-2018 CERN.

First, hydrogen is inserted in a strong magnetic field, where it is ionised. The protons are injected into the LINAC2, which accelerates them up to an energy of 50 MeV. They are then injected into the proton-synchrotron (PS) booster and subsequently into the PS, where they are accelerated to 1.4 GeV and 25 GeV, respectively. After the PS, the protons are injected into the super-proton-synchrotron (SPS), which accelerates them to an energy of 450 GeV. Finally, the protons are injected into the LHC, where they are accelerated to their final energy.

The LHC is filled with 2808 proton bunches, each containing about $1.1 \cdot 10^{11}$ protons at the beginning of the fill. The bunches have a temporal spacing of 25 ns and move with velocities extremely close to the speed of light c. The acceleration process takes about 20 minutes.[2]

There are four major experiments ongoing at the LHC: ATLAS [57] and CMS [58], which are multipurpose experiments, LHCb [59], which specializes in b quark physics and studies CP violation, and ALICE [60], which studies heavy ion collisions and quark-gluon plasma.

[2]These are the design values from Refs. [55] and [57].

3.2. The ATLAS Experiment

ATLAS is one of the two multi-purpose detectors at the LHC at CERN, searching for new physics and performing precision measurements in proton-proton (pp) collisions. Up to now, one of its most important achievements is the discovery of the Higgs boson together with the CMS experiment [20, 21]. This section gives a brief overview over the detector and its components. A more detailed description can be found in Ref. [57].

3.2.1. The Coordinate System

ATLAS uses a right handed coordinate system with the origin at the centre of the detector, which is centered at the interaction point 1 of the LHC. Using Cartesian coordinates, the positive x-axis is directed at the centre of the LHC ring, while the positive y-axis points upwards and the z-axis tangentially in the beam direction. Introducing spherical coordinates (r, ϕ, θ), the azimuthal angle ϕ is the angle of a particle in the transverse $x-y$ plane, while the polar angle θ is the angle from the beam axis. The r-coordinate stays as is.

The transverse momentum of a particle is defined as

$$p_T = \sqrt{p_x^2 + p_y^2}\,, \tag{3.1}$$

while the pseudorapidity η is defined as

$$\eta = -\ln\left(\tan\frac{\theta}{2}\right) = \frac{1}{2}\ln\left(\frac{|\vec{p}| + p_z}{|\vec{p}| - p_z}\right), \tag{3.2}$$

where $|\vec{p}|$ is the absolute momentum of the particle and p_z is its z component. The benefit of the pseudorapidity is that it is defined via the polar angle and that the particle flux in pp collisions per unit of pseudorapidity is approximately constant. In the high energy approximation, $m \ll |\vec{p}| \Rightarrow E \approx |\vec{p}|$, the pseudorapidity becomes an approximation of the rapidity y

$$y = \frac{1}{2}\ln\left(\frac{E + p_z}{E - p_z}\right). \tag{3.3}$$

Differences in the rapidity are invariant under Lorentz boosts along the z-axis. This is beneficial, as the LHC is a hadron collider and the centre-of-mass frames of its parton-parton collisions are boosted in the z direction.

Another important quantity is the distance in the $\eta - \phi$ plane

$$\Delta R = \sqrt{(\Delta\eta)^2 + (\Delta\phi)^2}. \tag{3.4}$$

This distance also is approximately invariant under longitudinal Lorentz transformations in the z direction, as the polar angle and differences in η are invariant under Lorentz transformations in the z direction.

3.2.2. Detector Components

With a length of 44 m, a height of 25 m and a weight of 7000 t, the ATLAS detector [57] is the largest detector at the LHC. It is cylindrical in shape and separated into a central barrel regions and two disc-shaped end-caps. The different detection systems are arranged in many concentric layers around the interaction point, so that the detector provides a nearly 4 π solid angle coverage around it. The inner layers are designed to measure the direction and momentum of charged particles, while the intermediate layers are composed of calorimeters to measure particle energies. The outermost layer measures the direction and momentum of muons. Between the inner layers and the calorimeters are magnetic solenoids in order to bend particle tracks for transverse momentum measurements. Also, there are three toroid magnets surrounding the calorimeters, one at the barrel and one at each end-cap. A cut-out image of the detector is shown in Figure 3.2.

The innermost part of the ATLAS detector, the inner detector, starts 3.1 cm away from the beam pipe. It consists of four components. The first component is the Insertable B-Layer [61]. It consists of silicon pixels with a size of 50 $\times$ 250 µm and was added in 2014 to improve the tracking performance and to cope with the expected higher radiation and hit occupancy in Run 2 of the LHC. The second component is a layer of silicon pixels with dimensions of 50 $\times$ 400 µm^2. The resolution in this detector is very high, as the environment near the beam pipe has a very high particle occupancy and many tracks need to be distinguished. The silicon pixels are surrounded with semiconducting silicon microstrip detectors with dimensions of 80 µm $\times$ 12 cm. The resolution is lower than for the silicon pixels, as the track density is significantly lower. The outermost part of the inner detector consists of a transition radiation tracker (TRT). It is made of gas-filled straw tubes with a diameter of 4 mm and a single gold-plated tungsten wire in each straw's centre, effectively combining a transition radiation detector with a proportional counter. In particular, pions can be distinguished from electrons using the TRT [62]. This is possible as the amount of transition radiation is dependent on the Lorentz factor $\gamma = E/m$. As electrons have a significantly lower mass m than pions, the Lorentz factor

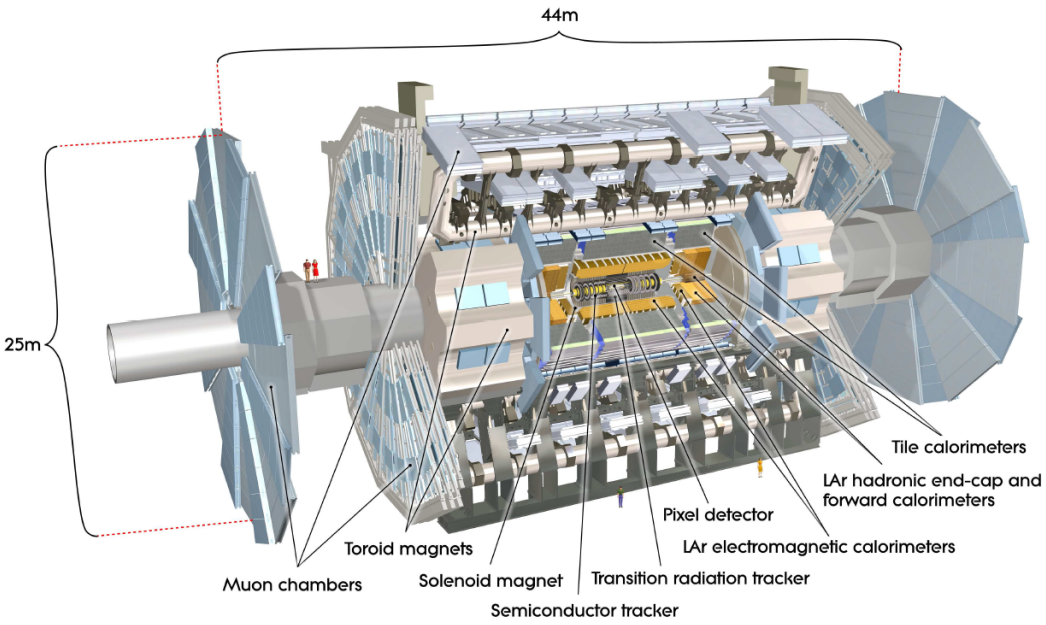

Figure 3.2.: Cut view of the ATLAS detector with labeled detector parts [57].

for electrons is higher than the one for pions at the same energy level. In consequence, electrons are much more likely to produce transition radiation, which can be used for particle identification.

The inner detector is embedded in a 2 T magnetic field, generated by the solenoid magnet. This field bends the trajectory of charged particles in the inner detector via the Lorentz force. The momentum resolution of the inner detector and the η coverage of the different components is listed in Table 3.1.

The next layers consist of the electromagnetic and hadronic calorimeters (ECAL and HCAL, respectively). Both calorimeters measure the energy of the particles by stopping them and absorbing all or most of their energy. In the ECAL, mostly electron and photon energies are measured, while the HCAL mostly measures hadron energies. If an electron or photon enters the ECAL, it will undergo Bremsstrahlung or pair production of electrons, respectively. This process will repeats until the energy of the particles is not sufficient to create Bremsstrahlung or electron pairs anymore and are absorbed, resulting in an electromagnetic (EM) shower. Typically, EM showers do not reach the HCAL. Hadrons will start interacting with the material and producing showers in the ECAL, so that they will both be contained in the ECAL and the HCAL. The ratio of energy between the two calorimeters together with the shower shape can be used to identify the type of the particle shower. In the HCAL, the hadrons will interact with the atomic nuclei of the calorimeter material. This mostly includes scattering of the hadrons at the nuclei or

Detector	Resolution	Coverage
Inner detector	$\sigma_{p_T}/p_T = 0.05\% \cdot p_T \oplus 1\%$	$\lvert\eta\rvert < 2.5$
ECAL	$\sigma_E/E = 10\%/\sqrt{E} \oplus 0.7\%$	$\lvert\eta\rvert < 3.2$
HCAL		
central region, end-caps	$\sigma_E/E = 50\%/\sqrt{E} \oplus 3\%$	$\lvert\eta\rvert < 3.2$
forward region	$\sigma_E/E = 100\%/\sqrt{E} \oplus 10\%$	$3.1 < \lvert\eta\rvert < 4.9$
Muon spectrometer	$\sigma_{p_T}/p_T = 0.05\%$ at $p_T = 1\,\text{TeV}$	$\lvert\eta\rvert < 2.7$

Table 3.1.: Transverse momentum and energy resolution and η coverage of the different components of the ATLAS detector [57]. The energy and transverse momentum are in GeV.

nuclear reactions. The interactions yield in hadronic showers, which can also have an EM component. Compared to EM showers, hadronic showers are broader and longer.

The ECAL is a sampling calorimeter that uses lead as passive and liquid argon (LAr) as the active material. The passive material usually is a material with a high proton number which will trigger a shower, while the active material produces the signal which is measured. The ATLAS ECAL has an accordion-like structure and a high granularity in order to provide a uniform response to the incoming particles. The HCAL is divided in three regions: the barrel part, composed of iron as absorber and plastic scintillator as active material, the end-cap part, composed of copper as absorber and LAr as active material and the forward region with tungsten as absorber and LAr as active material. The ECAL has a thickness of > 22 radiation lengths (X_0) at the barrel and of $> 24\,\text{X}_0$ at the end-caps. Including the HCAL, the detector has a thickness of about 9.7 interaction lengths (λ) at the barrel and of about $10\,\lambda$ at the end-caps. Adding the support structure, the detector has a total thickness of about $11\,\lambda$ at $\eta = 0$. The energy resolution of both calorimeters increases with the energy of the particle (see Table 3.1), as the more energy is carried by the particle, the larger the shower it creates.

The outermost layer of the ATLAS detector consists of an additional drift chamber tracking detector with a toroidal magnetic field produced by the toroidal magnets and three wheels at the end caps. The field has a strength of 0.5 T in the barrel and of 1 T in the end cap region, respectively. This layer provides an additional measurement for muons, which are minimally ionising particles in the energy regimes at ATLAS. Thus, they merely interact with the ECAL and HCAL and only leave tracks in the inner detector and these so-called muon chambers. As the muon chambers are quite large, they provide an additional precise measurement of the muon transverse momentum.
The resolution and coverage for all detector components is summarised in Table 3.1.

3.2.3. The Trigger System

As stated in Section 3.1, there is a bunch crossing and thus an interaction in the ATLAS detector every 25 ns. This is equivalent to an event rate of 40 MHz or a data rate of 600 Tb/s. Current technology is unable to handle and store such high rates of data. For this reason, ATLAS has a trigger system only allowing events of interest to be recorded. The trigger system is composed of the level-1 trigger (L1) which is hardware based and the high level trigger (HLT) which is software based [63]. The L1 trigger uses calorimeter and muon chamber information to search for events with a high energy deposit in the detector or with high-p_T muons. This step reduces the event rate to about 100 kHz [63]. The HLT takes these events and reconstructs the regions selected by the L1 using online reconstruction. Thus, different particles can be detected and it is possible to apply particle-specific cuts – triggers – on the event. In this way, the HLT reduces the event rate to about 1 kHz. All events passing the HLT are stored for offline analysis.

3.3. MC Generators

Predictions from theory are essential to any experiment, as its actual outcome must be compared to the expected one in order to be able to make scientific statements. This is of course also true for the precision measurements and searches for new particles which are conducted at ATLAS: To be able to compare the collected data to the SM or to BSM theories, a precise knowledge of the respective signal and background signatures is needed. On the other hand, the usage of hadron instead of lepton colliders complicates the calculations necessary to make these predictions, as the event structure is significantly more complex with $\mathcal{O}(1000)$ of particles per event. The resulting multi-particle multi-dimensional processes can only be calculated using Monte Carlo (MC) integration, implemented in MC event generators. The basic principles of MC generators [64, 65] are discussed in this section. The ATLAS-specific usage of MC generators and the corresponding infrastructure is presented in Ref. [66].

In general, the simulation of a hadron-hadron collision follows several separate steps. The calculations for each step can be processed separately. A sketch showing these different steps is shown in Figure 3.3. The first step is the computation of the cross section of the respective hard scattering event. For this, the matrix element (ME) of the process must be calculated. This calculation is performed at a certain order in perturbative QFT, usually at leading order (LO), and currently for some processes up to next-to-next-to-leading order (NNLO). The ME squared is interpreted as a probability amplitude for the process and with it, the cross section of the process can be calculated. Additionally, the

fact that hadrons are collided must be taken into account in this step. As hadrons are not elementary particles and their partons will actually drive the hard scattering event, the parton distribution functions (PDFs) must be included in the calculation. The PDFs describe how likely it is to find an elementary particle inside the hadron at a certain momentum fraction of the hadron. They can simply be multiplied with the original term from which the ME is calculated from, including an integration over the parton momentum share.

The second step is the inclusion of QCD and EW corrections to the hard scattering event. While QCD corrections can be quite large, due to the strong coupling of the strong force, while the EW corrections usually are much smaller. More precisely, the QCD corrections include final state and initial state radiation (FSR / ISR). This radiation consists of quarks or gluons, which are radiated from other quarks or gluons in a collinear or infrared manner with a large probability while conserving flavour, four momentum and unitarity. In addition to the ISR and FSR, radiation from secondary scattering of hadrons must be added to the event. These scattering processes either can occur by other partons from the same hadrons of the primary event, or from the collision of other hadron-hadron pairs from the same bunch. Together, all these particles form the parton shower, shown as the red, purple and yellow parts in Figure 3.3.

The third step is the hadronization of the partons. As QCD is confined, there can be no free states with colour charge, and all quarks and gluons from the parton shower will form colour-neutral states, i.e. mesons and bosons, which are then observed by the detector. There are two models to model the parton shower which are frequently used today: the string model and the cluster model. The string model is based on the assumption that the potential energy between a $q\bar{q}$ pair rises linearly with the distance between these quarks. As the partons from a hadron-hadron collision usually will have a high momentum, they move apart at nearly the speed of light, and at some point, the potential energy of the spanned field will be large enough to produce a light quark pair. This process goes on with including the newly produced quarks, up to a point where the quarks do not possess enough energy anymore to tear themselves apart from their partner, effectively forming mesons and baryons. Gluons are included as kinks on the flux tube between the two initial quarks. The cluster model is based on the preconfinement property of QCD. This means that color singlet states of partons, called clusters, are formed by the partons at each point of the parton shower. If such a cluster has a mass below $3 - 4\,\mathrm{GeV}$, it is transformed into hadrons through a two-body decay. Otherwise, the cluster undergoes a non-perturbative splitting process.

The fourth step is the simulation of the detector response to the simulated event. This

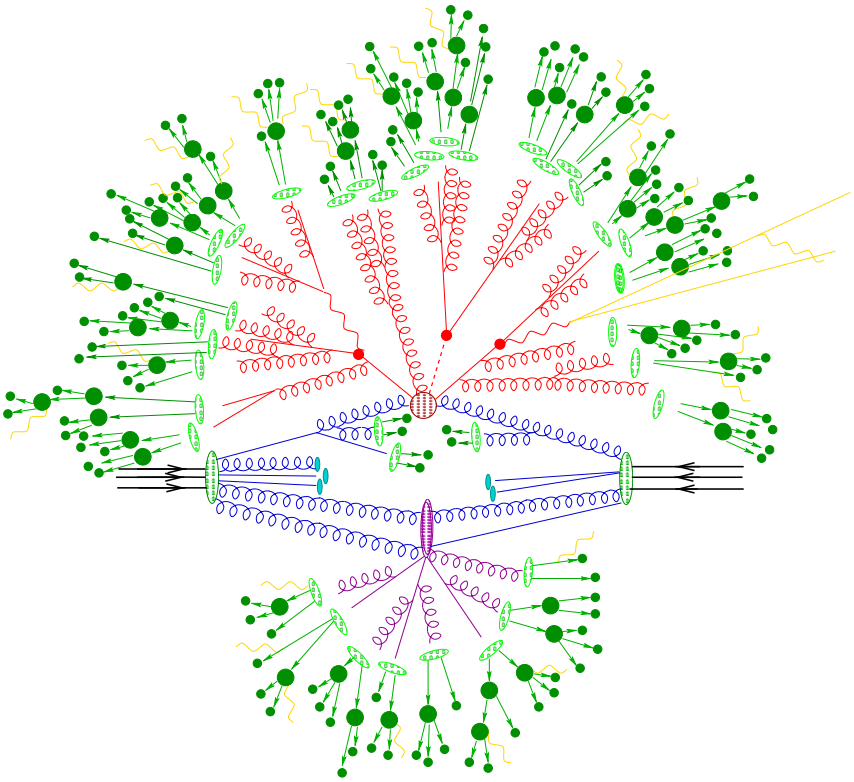

Figure 3.3.: Sketch of hadron-hadron simulation as simulated by a MC event generator [64]. The incoming hadrons are shown in black and the interacting partons in blue. The red blob in the center represents the hard scattering event, surrounded by the parton shower. A secondary hard UE is drawn in purple. The light green blobs indicate parton to hadron transitions, while the dark green represent hadron decays. Electromagnetic interactions are shown in yellow.

is necessary so that the simulated events can be compared to the collected data, which are collected with a physical detector. It is either possible to simulate the detector response using a full simulation modeled with GEANT 4 [67] or using a fast simulation, AFII [68]. While the full simulation is computing intensive and rather slow, as it simulates every component of the detector in detail, the fast simulation is about ten to twenty times faster [69]. It uses only a full simulation of the inner detector and the muon calorimeters, and relies on FastCaloSim [70] for the calorimeter simulation. FastCaloSim parametrizes the energy profiles of the parton shower in both longitudinal and lateral direction, and is much faster than a full calorimeter simulation.

3.4. Jets

When the partons hadronize, they each form a stream of mesons and baryons that reach the detector. Inside the detector, they will interact with the detector material, leaving tracks in the tracking detector and forming showers in the calorimeter systems. A jet ideally is the collection of all the tracks and calorimeter deposits originating from one parton. However, in experiment, it is not trivial to distinguish which track or calorimeter cluster should be associated with which parton. Therefore, different jet reclustering algorithms have been developed [71–75]. For the most part, these are bottom-up sequential algorithms starting at single particle level, clustering the single particles into a jet. The most common algorithms are the Cambridge/Aachen, k_T, and Anti-k_T algorithm. They use a similar formula to calculate the distance of particles to each other in order to decide which particles to combine in the same jet. The only difference between these algorithms is how the transverse momentum of the two particles influences their distance. Explicitly, the quantity

$$d_{ij} = \min\left(p_{T,i}^k, p_{T,j}^k\right) \frac{\Delta R_{ij}^2}{R^2}, \quad \text{where} \quad k = \begin{cases} -2 & \text{Anti}-k_T \\ 0 & \text{Cambridge/Aachen} \\ 2 & k_T \end{cases} \tag{3.5}$$

is defined. Here, k defines the type of the algorithm, while the parameter R controls the jet area. The indices i and j enumerate all constituents of the event. The distance ΔR uses the definition from Equation 3.4, only that instead of the pseudorapidity, the rapidity is used. For each pair of constituents in the event, the distance d_{ij} is calculated, as well as the distance of each constituent to the beam

$$d_{iB} = p_{T,i}^k \,, \tag{3.6}$$

where k is defined as in Equation 3.5. If the minimal d_{ij} is smaller than d_{iB}, the two constituents will be merged in a temporary jet, which will be added to a modified list of constituents, while the original constituents i and j are removed from this list. Otherwise, i is labeled to be a jet, and is removed from the list of constituents. This procedure is repeated until all constituents have been clustered.

The different powers of the algorithms have a significant impact on how the clustering procedures works. If $k = 2$, the clustering will start with the softest constituents of the event, i.e. the constituents with the lowest transverse momentum, being clustered to the closest particles. If $k = 0$, the momentum of the particle will have no influence on the clustering at all, and the nearest particles will be clustered together. If $k = -2$, the

clustering will start with the hardest constituents of the event, i.e. the constituents with the highest transverse momentum. In ATLAS, the default jet collection is clustered using Anti-k_T jets with a distance parameter of $R = 0.4$. These jets will be referred to as small-R jets (SRJ) in the following.

In this thesis, a boosted topology from the decay of a CP-even Higgs boson with a mass of $m_X = 2\,\text{TeV}$ into a pair of SM Higgs bosons with a mass of approximately 125 GeV is investigated. The Higgs bosons then either decay into two W bosons or two τ leptons. This yields a final state where the constituents of interest from different partons are rather close in the detector. Assuming a two body decay with massless products, the distance of the products can be approximated via

$$\Delta R \approx \frac{2m}{p_T}\,, \tag{3.7}$$

where m and p_T are the mass and the transverse momentum of the mother particle, respectively. Given the mass scales that have been mentioned, the approximate distance between two quarks originating from a W boson can be given by

$$\Delta R \approx \frac{2m_W}{p_T^W} \approx \frac{2m_W}{\frac{1}{2}m_X - m_W} \approx 0.2\,. \tag{3.8}$$

The jets originating from these partons cannot be resolved using the standard SRJ algorithm. Instead, larger jets with a size parameter of $R = 1.0$ can be used to include all decay products from the hadronic W decay in their reconstruction. These are referred to as large-R jets (LRJ) in the following. The reconstruction of the boosted τ lepton pair does not explicitly rely on LRJs and is explained in Section 3.5.

With the greater area of the jet, much unrelated radiation is picked up together with the desired particles from the hard scattering partons. To reduce this radiation content, the LRJ is reclustered using the k_T algorithm with a distance parameter of $R = 0.2$. This clusters the soft jet constituents from pile-up together first. Then, all subjets which possess less than 5% of the total transverse momentum of the LRJ are removed from the jet collection, and a LRJ with reduced pile-up content remains.

Given that LRJs can be seeded by particles originating from one parton, or multiple partons, substructure information is often used to distinguish signal over background events. Many variables have been developed for this purpose, for example N-subjettiness [76] or energy correlation functions [77] and ratios thereof [77–79].

3.5. Di-Tau Jets

The two τ Leptons from the decay of the second SM Higgs boson will also be close in the aforementioned signal topology, just as the quarks from the hadronic W boson decay. This cannot be handled by the single τ lepton reconstruction algorithm, as it uses the standard ATLAS SRJ as an input seed. The solution again is to reconstruct the two τ leptons with a LRJ. Such a LRJ containing two τ leptons will be referred to as a Di-Tau jet. The single τ leptons can be accessed via accessing the subjets of the Di-Tau jet. However, a method for identification and background discrimination must be applied on the Di-Tau jet, as electrons or QCD jets can be misidentified as hadronically decaying τ leptons [80].

To reconstruct the Di-Tau jets, a list of LRJ with transverse momentum larger than 15 GeV is considered. These candidates are then scanned for subjets using the Cambridge/Aachen algorithm with a distance parameter of $R = 0.2$. The leading and subleading subjet, i.e. the two subjets with the largest momentum, are assumed to contain the two τ leptons. Tracks are associated to the Di-Tau jet and its subjets if they are within their respective jet area, i.e. within a distance closer to the (sub)jet than the respective R. Subjets with more than four associated tracks are rejected to suppress QCD jet background. The Di-Tau jet candidates are required to contain at least two subjets which each have at least one associated track. The four momentum of the Di-Tau jet candidate is then set to be the sum of the four momenta of the two leading subjets. Finally, a boosted decision tree is trained in order to provide an identification variable for Di-Tau jets and discriminate the Di-Tau jet against QCD jet background [80]. There are four possible working points (WP) of the Di-Tau jet ID: very loose, loose, medium, and tight. As shown in Figure 3.4, the method is shown to reconstruct and identify boosted τ lepton pairs with a momentum of up to 1200 GeV with a high efficiency. However, if the τ lepton pair has a combined transverse momentum of less than 500 GeV, the nominal single τ lepton reconstruction method should be preferred.

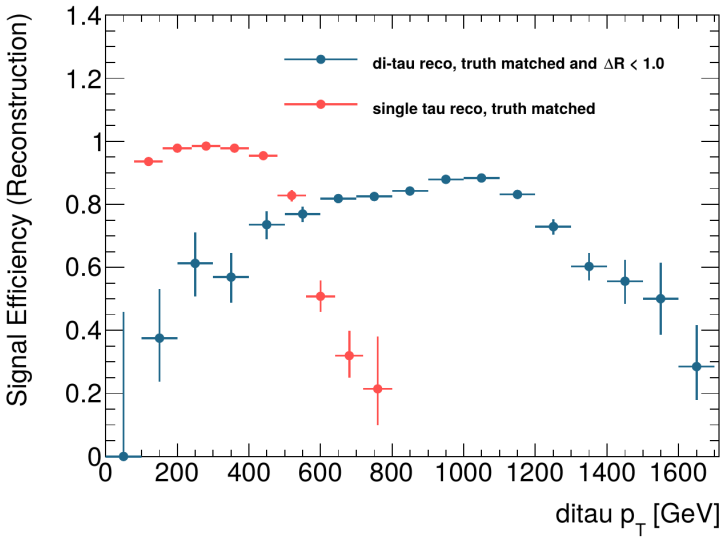

Figure 3.4.: Di-Tau and single-Tau reconstruction efficiencies as a function of Di-Tau p_T [80]. The Di-Tau reconstruction algorithm extends the sensitivity for τ pair reconstruction to up to 1200 GeV.

4. Analysis

In this chapter, the investigation of the boosted $pp \to X \to HH \to WW\tau\tau$ topology is discussed. As the presented channel and topology have never been analysed before, the methods for the generation of new Monte Carlo (MC) samples are presented and validation plots for these samples are shown. A shape comparison of leading order (LO) and next to leading order (NLO) distributions is conducted. Also, the technical setup for the analysis is presented. Finally, the selection of an optimized set of cuts for signal and background separation is conducted.

4.1. Event Topology

As discussed in Section 2.2.4, the boosted $HH \to WW\tau\tau$ channel is investigated, such that the Higgs boson pair originates from a heavy CP even scalar resonance, X, as predicted by a 2HDM. Specifically, the analysis is focused on the $1\,\ell + \text{jets}$ final state, such that the lepton comes from the decay of a W boson. In this context, lepton only refers to electrons and muons. A lab-frame diagram of this process is shown in Figure 4.1. The topology offers a distinct signature with two approximately back to back LRJs where one has a lepton in close proximity. This is expected to provide a good suppression of mul-

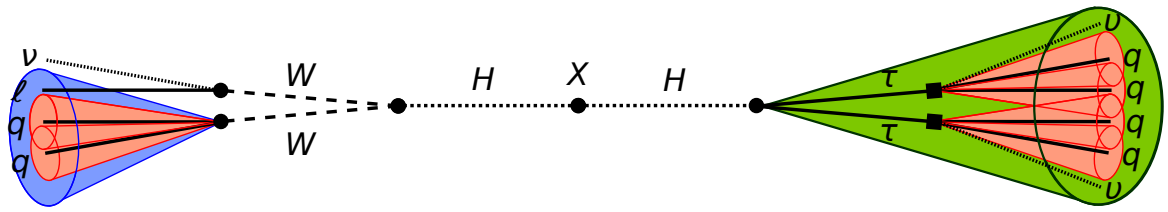

Figure 4.1.: Sketch of the process $pp \to X \to HH \to WW\tau\tau \to \ell\nu_\ell qq\nu_\tau qq\nu_\tau qq$ in the centre of mass frame of the heavy resonance X. The red cones denote SRJs while the blue and green cones represent LRJs. Adapted from Ref. [81].

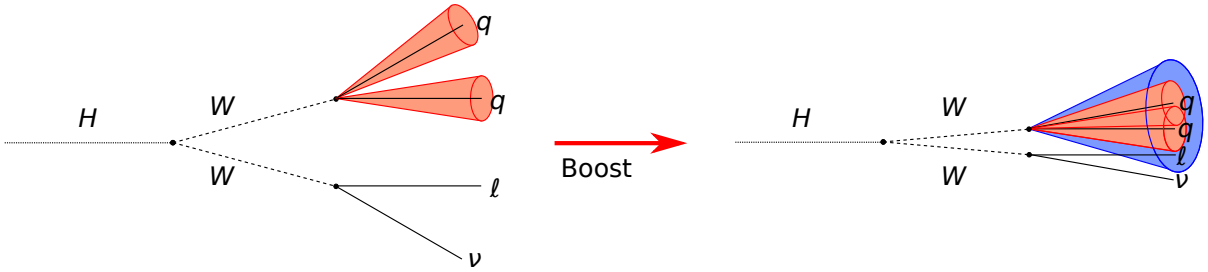

Figure 4.2.: Effect of the boost on the distance between the Higgs boson decay products on the W boson side due to the decay of a heavy resonance. The same effect applies for the products on the τ lepton side. Adapted from Ref. [81].

tijet backgrounds. Also, the use of hadronic Di-Tau taggers offers excellent background suppression for this topology [80]. However, due to the fact that neutrinos are present in both the decay of the W bosons and the τ leptons, a complete reconstruction of the event is not feasible.

This thesis investigates the $WW\tau\tau$ final state in a boosted topology. The boost of the products is due to the mass difference between the heavy resonance and the products, which is transformed into kinetic energy. The higher the mass of the heavy resonance, the higher is the boost of the products, and the smaller is the angular distance between them, i.e.

$$\Delta R_{WW/\tau\tau} = f(M_X, p_T^H) \approx \frac{2m_H}{p_T^H}\,. \tag{4.1}$$

This effect is depicted in Figure 4.2, sketching the application of a boost to a $H \to WW \to qq\ell\nu$ decay. With a sufficient boost, the decay products can all be reconstructed by one LRJ.

While such a signature is beneficial to suppress backgrounds if cuts on the LRJ are applied, it also comes with challenges. Techniques for tagging and analysing Di-Tau objects and LRJs [76–78, 80, 82] are well-established in ATLAS, but the possible overlap of objects in the detector is an issue: in many cases, the event topology results in a lepton overlapping with a LRJ. In order to keep both the hadronic component of the LRJ and the lepton without double counting the detector signature, a novel overlap removal (OLR) technique must be applied to the analysis. Such an adapted OLR for leptons near LRJs has been developed in Ref. [81]. This OLR will be used in this analysis, together with an OLR dealing with LRJs and Di-Tau objects, and is discussed in Section 4.6.

The most important backgrounds for this topology are expected to be WW + jets and $Z \to \tau\tau$ + jets. Possible other backgrounds to be considered are W + jets, WZ + jets, ZZ + jets, $t\bar{t}$, $t\bar{t}H$, $H \to \tau\tau$ via ggF and VBF, WH, ZH, and multijet events. These

backgrounds are grouped in six general categories: single boson (V), diboson (VV), QCD (jj), vector boson with associated Higgs boson (VH), $t\bar{t}$, and $t\bar{t}$ with associated Higgs boson (ttH). The contributions of these backgrounds to the analysis are estimated using MC generated samples.

4.2. Sample Generation

New MC samples need to be generated in order to simulate the signal signature in the detector. For this purpose, both LO and NLO job options (JO) are created. The JO are used to tune the MC generators, so that they simulate the wanted processes and final states. The generation uses a heavy resonance mass list from 0.5 up to 3 TeV with seven mass points: $m_X/\text{TeV} \in \{0.5, 0.75, 1.0, 1.5, 2.0, 2.5, 3.0\}$. To allow for a possible future use of the produced samples or JOs in other analyses such as the investigation of multilepton topologies, the topology of the samples is chosen to contain events with at least one prompt lepton without a requirement on the origin of the lepton. As the current standard for ATLAS HH MC samples uses LO, the official request for MC samples used the prepared LO JOs for a heavy resonant mass of 2 TeV.[1] For the validation, samples containing 5000 events per mass point are generated at truth level[2] for LO and NLO. The TRUTH1 derivation is used for the derivation of the corresponding derived analysis object data (DAOD) files. The TRUTH1 derivation contains the entire record of truth particles, i.e. the PDGID [26], information on which particles are the parents and children and the exact four vector of each particle in the event. All plots shown in Section 4.3 are truth level plots.

4.2.1. Generator Settings

The LO samples are produced using MadGraph5_aMC@NLO 2.3.3 [83]. For the parton shower, hadronization and underlying event (UE), MadGraph was interfaced with Pythia 8.212 [84]. For both MadGraph and Pythia, the NNPDF2.3 LO parton distribution function (PDF) set [85] is used. Also, the A14 set of tuned UE parameters [86] is used. For the 2HDM theoretical model, the HeavyHiggsTHDM [87] is used.
The NLO samples are produced using MadGraph_aMC@NLO 2.2.3. The parton shower,

[1] As the number of events for samples for new channels in the ATLAS HH group is limited, it would not make sense to request more than one sample for the first feasibility study – requesting more samples would potentially lower the absolute yields of each sample down to a level where no proper analysis is possible anymore.

[2] Truth level means that all properties of all particles in the event are precisely known, i.e. the full decay chain and all kinematic properties. Also, it does not include a detector simulation.

hadronization and UE are simulated using Herwig++ 2.7.1 [88]. MadGraph uses the PDF set CT10 [89] for the ME calculation, while Herwig uses the CTEQ6L1 PDF set [90]. Additionally, the UE-EE-5 set of tuned UE event parameters [91] is used. The 2HDMCP_EFT model is used as 2HDM theoretical model [87].
The narrow width approximation is used for the heavy resonance in the LO as well as in the NLO sample generation. Also, both the LO and NLO samples use filters to ensure that the samples only contain events with the $X \to HH \to WW\tau\tau \to 1\ell + \text{jets}$ topology. This is cross-checked by producing various multiplicity plots of particles originating from the heavy resonance, e.g. the multiplicity of Higgs and W bosons and τ leptons.

4.3. Sample Validation

Selected kinematic distributions will now be shown from the validation of the LO samples, while the plots shown from the NLO samples concentrate on validating the boosted nature of the topology. Finally, a shape comparison of the LO and NLO samples again focuses on kinematic distributions.

As shown in Figure 4.3a, the invariant mass of X is well simulated in the distribution of its decay products. The generated mass points peak at the desired value. Figure 4.3b shows the p_T of the HH system calculated from the addition of the H boson 4-momenta.

The ΔR separation between various pairs of objects is shown in Figure 4.4. In Figures 4.4a and 4.4c, the ΔR distributions are shown for τ leptons, while in Figures 4.4b and 4.4d, the ΔR distributions are shown for the W bosons. The upper figures show the ΔR distributions between the two W bosons or the two τ leptons, while the lower figures show the ΔR distributions between the lepton and the closest SRJ if the lepton is produced in a W boson or τ lepton decay, respectively. The closest SRJ is nearly always a jet from the hadronically decaying τ lepton or W boson.

As clearly visible from all four plots, the angular separation between the direct Higgs boson decay products as well as the distance between the subsequent products of the Higgs boson decay products decreases with an increasing mass of the heavy resonance. This behaviour is expected for the boosted topology. Transferring this to the reconstruction which will be done in real data, where the two τ leptons start to regularly overlap at a resonant mass of about 0.75 TeV, as the standard τ lepton reconstruction algorithm reconstructs τ leptons in a cone with size parameter $R = 0.4$ [92]. The overlap becomes critical at a heavy resonance mass close below 1.5 TeV (see Figure 4.4a), where the two τ leptons are usually closer than $\Delta R = 0.4$. This is also the case for the distance of the lepton from τ lepton decays to the closest jet: Starting at a resonance mass of about

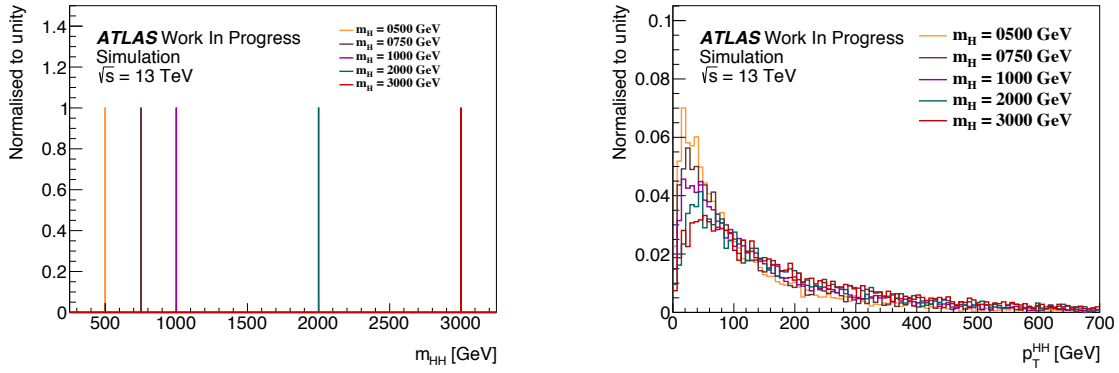

(a) *(b)*

Figure 4.3.: (a) Invariant mass and (b) transverse momentum of the HH system for a selection of the generated mass points at LO.

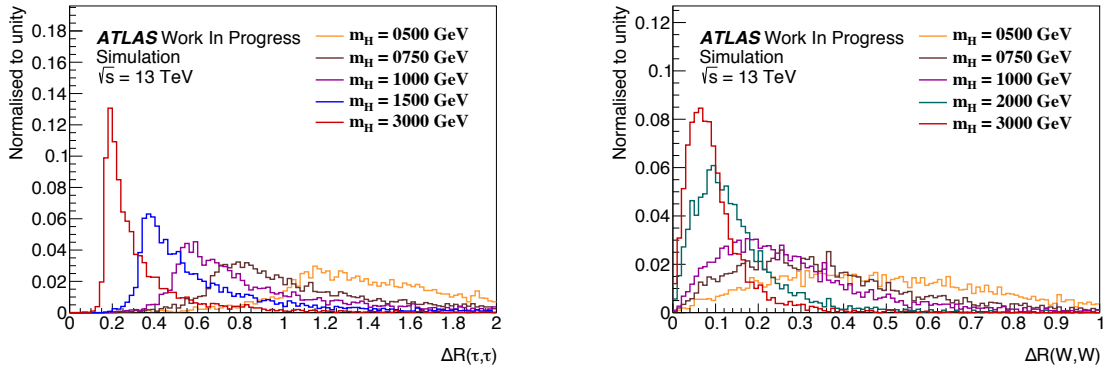

(a) *(b)*

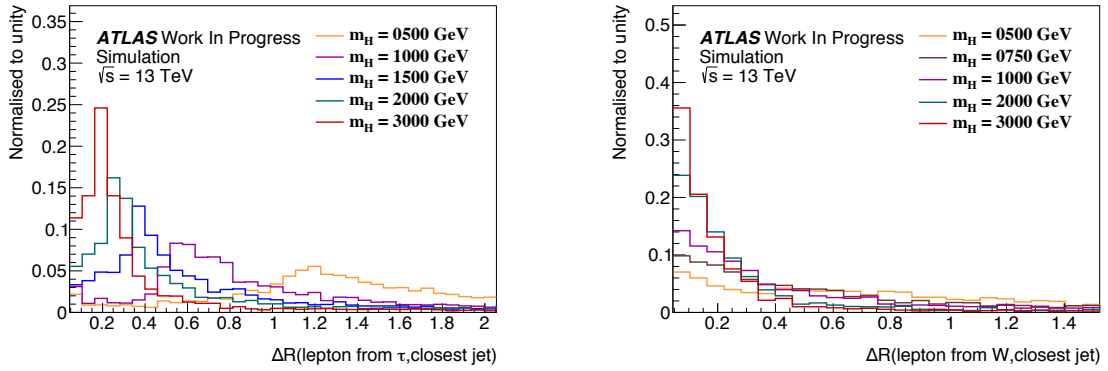

(c) *(d)*

Figure 4.4.: Distances in ΔR between (a) the two τ leptons, (b) the two W bosons, (c) the lepton if the lepton is on the τ lepton side and the closest SRJ, and (d) the lepton if the lepton is on the W boson side and the closest SRJ for a selection of the generated mass points at NLO. The closest SRJ nearly always is the jet originating from the hadronically decaying τ lepton or W boson.

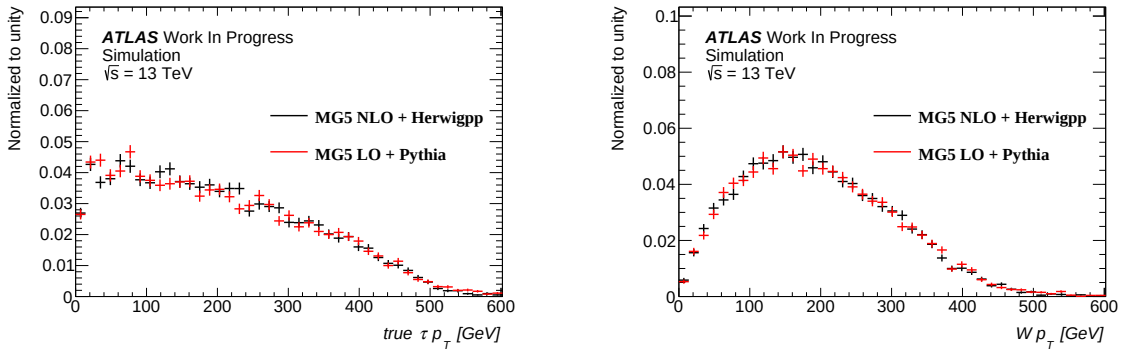

(a) *(b)*

Figure 4.5.: Shape comparisons of LO and NLO samples for $m_X = 1\,\text{TeV}$. Figure (a) shows the transverse momentum of the τ lepton, while Figure (b) shows the transverse momentum for the W bosons. The distributions only deviate within statistical fluctuations.

1.5 TeV, the lepton will usually be inside the hadronically decaying τ lepton cone.

A similar effect can be observed for the two W bosons, although the effect already becomes of importance at lower resonance masses of about 0.5 TeV and between 0.5 and 0.75 TeV, respectively. Intuitively one would expect that the τ leptons should always be less separated for the same resonance mass, as they are much lighter than the W bosons and thus can be more boosted. However, this also means that the τ leptons carry much more transverse momentum relative to the Higgs boson momentum. The hypothesis is that this results in the W bosons being more collinear with the Higgs boson, yielding a smaller angular separation of the W bosons than of the τ leptons.

Finally, a shape comparison between LO and NLO samples was conducted at a heavy resonant mass of 1 TeV. This is done in order to ensure that no unexpected effects occur when transitioning from LO to NLO sample generation. Two example plots showing the distribution of the true τ lepton p_T and the distribution of the W boson p_T are shown in Figure 4.5a and 4.5b, respectively. While the shapes of the LO and NLO distributions are similar and only differ in slight statistical fluctuations, a difference in the p_T of the τ lepton in comparison to the p_T of the W boson can be observed. The difference is consistent with the observation discussed in the previous paragraph, that the angular separation between the W bosons seems to be smaller than between the τ leptons for the same resonant mass.

4.4. Analysis Setup

Technical Setup

In Run 2 of the LHC, ATLAS uses three main data formats to store events which will be used for analysis: xAODs, DxAODs, and n-tuples.

xAODs xAODs are the most general data format used in ATLAS, both for simulated and collected data. In these, all reconstructed objects and underlying information from all events saved in the data stream are stored. Thus, xAODs are the largest data format.

DxAODs DxAODs (derivations), i.e. derived xAODs, are analysis-group-specific xAODs. In contrast to the original xAODs, they do not contain the full event information, but are optimized to contain the information that is needed for analyses conducted by the specific groups. For this, variables, events and/or objects which are not needed are removed from the samples, while new variables or objects derived from the original information contained in the original xAOD can be added. The samples used in this analysis are derived using the HIGG4D6 derivation, which is described below.

n-tuples n-tuples are usually used to store analysis-specific variables calculated from the analysis-group-specific DxAODs. They store the data as tuples in branches of variables. In comparison to the DxAODs, they are even further reduced in size, as they only contain variables needed for the specific analysis. The processing of n-tuples in comparison to the DxAODs is usually faster, as many time consuming calculations already have been conducted in the production of the n-tuples. This is also the data format which is commonly used for the production of histograms.

As the general framework for the analysis, ROOT [93] is used. It provides a rich amount of tools and frameworks useful for analyses in high energy physics. The derivation used for the production of DxAODs is HIGG4D6. This derivations requires an event to have at least two LRJs with $p_T > 300\,\text{GeV}$ and at least one Di-Tau jet with $p_T > 300\,\text{GeV}$. Additionally, it requires the events to have triggered a LRJ or a single lepton trigger. For the production of the n-tuples, a standalone self-made framework written in C++ is developed on the basis of the EventLoop software class. To find the optimal selection cuts and produce the histograms and cutflow, ROOT-based scripts are used. HistFactory [94] is used for the limit setting.

Process	# generated events	Cross section @ 13 TeV / [pb]	Generator
W	403,478,000	6.02×10^4	Powheg + Pythia8
Z	396,035,000	5.66×10^3	Powheg + Pythia8
WW	38,495,000	55	Powheg + Pythia8
WZ	44,434,000	21	Powheg + Pythia8
ZZ	18,298,000	5.0	Powheg + Pythia8
WH	200,000	1.1	Pythia8
ZH	200,000	0.6	Pythia8
jj	348,470,000	2.46×10^9	Pythia8
$t\bar{t}$	193,918,000	832	Pythia8
$t\bar{t}H$	9,980,000	0.22	MadGraph5

Table 4.1.: List of all considered background processes with the respective number of generated events, the cross section and the used generator. The full list of used samples can be found in Tables A.1 to A.3 in the appendix.

Background Samples

The background contribution consists of various SM processes which are included in the analysis via MC generated samples. The single and diboson samples are both generated using PowhegBox [95] with the CT10 tune for the calculation of the ME and Pythia8 with the AZNLO tune [96] and the CTEQ6L1 PDF set for the parton shower. The VH samples as well as the dijet and $t\bar{t}$ samples are generated using Pythia8 both for the calculation of the ME and for the parton shower, using the A14 tune and the NNPDF23LO PDF set, respectively. The top pair and associated Higgs boson samples are produced using MadGraph5_aMC@NLO with the NNPDF30ME tune for the ME, while Pythia8 with the A14 tune and the NNPDF23 PDF set is used for the parton shower. All samples were produced using a full simulation of the ATLAS detector by GEANT 4. In Table 4.1, the number of events used for each background process is shown. The full list of used samples split by subprocesses can be found in Tables A.1 to A.3 in the appendix.

Weights

MC generators are not in perfect agreement with observed data, even for processes which are known to a good extent. For this reason, corrections need to be applied in order to match the generated distributions to measured data.

To begin with, the factor

$$\frac{w_{MC}}{\sum\limits_{\text{Events}} w_{MC}} \tag{4.2}$$

takes the individual MC weights w_{MC} and the total weighted number of MC events $\sum_{\text{Events}} w_{MC}$ into account: First, it corrects the single event by its MC weight, which takes NLO loop corrections and interference into account, and second, it ensures that the total number of weighted events on xAOD level is normalized to unity. Then, the number of generated events must be normalized to the expected amount of data collected in the investigated data taking period. This is done by weighting each event with a factor of $\sigma \times \mathcal{BR} \times \int \mathcal{L} \mathrm{d}t$, where the cross section σ and the branching ratio $\mathcal{BR}$ are predicted by theory and the integrated luminosity $\int \mathcal{L} \mathrm{d}t$ corresponds to the data taken for the current analysis.

The MC production filter efficiency ϵ also needs to be taken into account. ϵ is defined as the fraction of generated events that pass the truth-level criteria, which, in this analysis, are used to select the at least one lepton topology. Thus, it normalizes the $HH \to WW\tau\tau$ cross section to the cross section of the selected $HH \to WW\tau\tau \to \geq 1\ell$ final state.

Together, this yields the final event weight

$$w = \frac{\sigma \times \mathcal{BR} \times \int \mathcal{L} \mathrm{d}t \times \epsilon \times w_{MC}}{\sum_{\text{Events}} w_{MC}} \,. \tag{4.3}$$

In this analysis, a luminosity of $\int \mathcal{L} \mathrm{d}t = 150\,\mathrm{fb}^{-1}$ is assumed. This approximately matches the anticipated full dataset of the ATLAS experiment collected in the years 2015 to 2018. The cross sections and branching ratios for all SM processes used in this analysis are calculated from SM predictions [32, 97]. For the signal process, $pp \to X \to HH$, a cross section of $\sigma_{\text{signal}} = 10\,\mathrm{fb}$ is assumed, based on the latest upper limits to this cross section set by the search for two Higgs bosons in the $b\bar{b}b\bar{b}$ final state [97]. The cross sections and branching ratios for all processes are summarized in Table A.3 in the appendix.

In a full analysis, further weights should be included in addition to the above. On the one hand, this regards the vertex weight and the pile-up weight, correcting for the modeling of the z-position of the primary vertex and the generation of the pile-up profile, respectively.

In addition, corrections for the MC modelling of particle ID need to be applied. These are used in order to correct the expected ID efficiency from MC generation to the actual efficiency found in data. However, these weights were not included due to technical reasons and time constraints. As the weights are assumed to be approximately 1, this should only have a small effect on the final result of the analysis, which is negligible in comparison to the other uncertainties.

4.5. Object Definitions

There are five different types of objects used in this analysis: Electrons, Muons, Di-Tau jets, LRJs, and SRJs. While the four former appear directly in the final state and are used for variable calculation and to enforce constraints, the latter is only used to apply a b-jet veto in the preselection. All objects must fulfill individual conditions in order to be accepted into the analysis, i.e. identified. These conditions are referred to as identification (ID) requirements. A looser ID requirement results in a higher acceptance of object candidates, however, at the same time the purity of the selection will drop.

Electrons Electrons [98] are reconstructed by matching tracks from the inner detector to energy deposits in the ECAL. They are required to have medium ID quality, and must have a transverse momentum of $p_T > 10\,\text{GeV}$. Also, they are required to be in an η range of $|\eta| \in ([0, 1.37] \cup [1.52, 2.47])$, which excludes the transition region between the central barrel and the end-caps of the calorimeter (crack region), where the reconstruction information is much less reliable than in the rest of the detector.

Muons Muons [99] are reconstructed with information from the inner detector and the muon spectrometer, as they leave little energy in the ECAL and HCAL. The reconstruction is conducted in both subdetectors, and the separate results are then merged to get the final reconstructed muon. As for electrons, a transverse momentum of $p_T > 10\,\text{GeV}$ is required. The η range is restricted to $|\eta| < 2.7$, as muons are not effected by the calorimeter crack region. Overall, muons are required to pass the medium ID quality criterion.

LRJ This analysis uses LRJ [100] from the standard jet collection described in Section 3.4. These LRJ are reconstructed using local hadronic calibrated topological clusters from the ECAL and HCAL. These clusters are individually calibrated in order to reflect or compensate the calorimeter response and signal losses due to dead material or malfunctioning detector parts, respectively. They are required to have a transverse momentum of $p_T > 200\,\text{GeV}$ and must have $|\eta| < 2$, as the jet object as a whole can only be calibrated in this detector region.

Di-Tau Jets The reconstruction of Di-Tau jets is described in Section 3.5. They are required to pass the very loose ID criterion and have a minimal transverse momentum of $p_T > 300\,\text{GeV}$. Also, they are required to have $|\eta| < 2$ and must have at least two subjets. The former is a relic of the Di-Tau jets being seeded by LRJs, while the latter is to favor

Di-Tau jets with two hadronically decaying τ leptons versus Di-Tau jets with only one hadronically decaying τ lepton.

SRJ SRJ [101] are not used as signal objects in this analysis, however, they play a crucial role in identifying b-jets. This is important to apply a b-jet veto to the events in order to suppress background processes containing t-quarks. SRJs are required to have a transverse momentum of $p_T > 20\,\text{GeV}$ and must have $|\eta| < 4.5$. The standard jet collection AntiKt4EMTopoJets is used.

4.6. Overlap Removal

When reconstructing objects in ATLAS, the corresponding reconstruction algorithm for each object is run separately on each event, and therefore the same particle can be reconstructed as multiple objects. Therefore, there can be overlapping objects in a given event. Before conducting any analysis, the used objects must thus be scanned for overlaps, and if any overlap is found, the ambiguity must be removed. The overlap removal (OLR) used in this analysis is presented in this chapter. It combines elements of the OLR used in a search for boosted $HH \to \gamma\gamma WW$ events [81] with OLR constraints derived from properties of Di-Tau jets [80, 102].

First, the overlap between electrons and SRJs is resolved. On the one hand, electrons produce EM showers in the ECAL, which can be misidentified as SRJ. On the other hand, a SRJ can contain non-prompt electrons from EM decays. The SRJ is removed if $\Delta R(e, \text{SRJ}) < 0.2$ is fulfilled. To account for the boosted nature of the topology, electrons are allowed to be closer to SRJs if they have high transverse momentum. They are removed if

$$\Delta R(e, \text{SRJ}) < \min\left(0.4, 0.2 + \frac{10\,\text{GeV}}{p_T^e}\right) \tag{4.4}$$

is satisfied. The OLR between muons and SRJs is similar to the one used for electrons and SRJs. The difference here is that muons are very unlikely to fake a SRJ, as they deposit only a minor part of their energy in the calorimeters. Thus, SRJs will not be removed if they are found to be close to a muon. However, muons are removed from the event if the distance to the SRJ satisfies

$$\Delta R(\mu, \text{SRJ}) < \min\left(0.4, 0.04 + \frac{10\,\text{GeV}}{p_T^\mu}\right). \tag{4.5}$$

An OLR between electrons and muons is also conducted. If an electron is found near a muon, $\Delta R\,(e, \mu) < 0.2$, it is removed.

Di-Tau jets have a large overlap with LRJs due to the implementation of the Di-Tau jet reconstruction method. Thus, only the Di-Tau jet which is assumed to be the signal Di-Tau jet is used in the OLR with the LRJ and all other Di-Tau jets are discarded.[3] Any LRJ which has a distance to this Di-Tau jet of $\Delta R\,(\text{Di-Tau jet}, \text{LRJ}) < 0.5$ is removed from the event.

Furthermore, an OLR between electrons and both LRJs and Di-Tau jets is applied. The OLR between electrons and LRJs is taken from Ref. [81]. The LRJ is removed when the distance to an electron satisfies $\Delta R\,(e, \text{LRJ}) < 1$ and either

$$m_{\text{LRJ}} < 15\,\text{GeV} \quad \text{or} \quad \frac{p_T^e}{p_T^e + p_T^{\text{LRJ}}} > 0.8 \tag{4.6}$$

are fulfilled, i.e. if the mass of the LRJ is very small or if the electron carries most of the LRJ's momentum. The OLR between electrons and Di-Tau jets is derived from the fact that electrons are likely to fake τ leptons in the detector. Thus, e.g. an actual τ lepton close to an actual electron which is misidentified as a τ lepton could be misidentified as a Di-Tau jet. Therefore, the Di-Tau jet is removed if the distance of any of its subjets to an electron satisfies $\Delta R\,(e, \text{Subjet}_i) < 0.1$.

4.7. Object and Event Selection

First, the Di-Tau jet, the LRJ, and the lepton which are used as the signal objects must be selected. The Di-Tau jet is is simply defined as the Di-Tau jet with the highest Di-Tau jet ID score. If there is no Di-Tau jet in the event, the event is discarded. Then, the LRJ which has the highest transverse momentum is picked as the signal LRJ. If there is no remaining LRJ in the event, the event also is discarded. Finally, the number of electrons and muons in the event is checked. If the event contains exactly one electron or exactly one muon, this electron or muon is defined as the signal lepton. Else, the event is discarded.

In the event selection, cuts are used in order to differentiate signal and background events based on the expected event topology of the signal. In a first step, the event is required to have exactly one signal lepton, at least one Di-Tau jet, and at least one LRJ. In the following, this selection state will be referred to as the loose preselection.

On top of the loose preselection, the WP for the selection of the Di-Tau jet must be

[3] The selection process for the Di-Tau jet is described in Section 4.7.

Cut	Signal	Total Background	Significance Σ_A
Loose Preselection	1.203	44644.4	0.006
Tight Preselection	0.764	5055.54	0.011

Table 4.2.: Expected yields after the preselection on $150\,\mathrm{fb}^{-1}$ of data.

selected. In addition, the event is required to not have any b-jets in it (b-veto). In order to do this, b-jets need to be identified. For this, a WP must be selected, too. The selection of these two WPs is conducted using the same method as for the selection of the optimal set of cuts and is described in Section 4.9. The loose preselection together with the selected WPs for the Di-Tau jet ID and the b-veto are referred to as tight preselection. The event yields after loose and tight preselection are summarized in Table 4.2.

From the expected back-to-back nature of the signal topology, it seems that also a cut on the distance between the different selected signal objects offers a good background suppression. However, it was decided not to apply such a cut. The details of this decision are discussed in Section 4.9.

4.8. Optimization Variables

In this section, variables which yield a good separation power between signal and background events are described. The variables are:

- The transverse momentum p_T of any of the signal objects, i.e. the Di-Tau jet, the LRJ, or the lepton. As all of these objects result from a decay of a high mass particle, they are likely to carry a higher amount of energy than similar objects found in the background. The distribution of the transverse momentum of these objects after the loose preselection for signal and background is shown in Figures 4.6 to 4.8.

- The sum of the transverse momentum of all signal objects,

$$H_T = p_T^{\ell} + p_T^{\mathrm{LRJ}} + p_T^{\text{Di-Tau jet}} \,. \tag{4.7}$$

  In the same way as the individual signal objects are expected to carry more energy than the single background objects, H_T is expected to be larger for signal than for background events. The distribution of H_T after the loose preselection for signal and background is shown in Figure 4.9.

- The missing transverse energy, E_T^{miss}, receives contributions from both the decay of the two W bosons and the decay of the two τ leptons, as in both decays neutrinos are

involved. Depending on how well the E_T^{miss} is balanced between these two decays, the E_T^{miss} can possibly be a good separation variable. The distribution of E_T^{miss} after the loose preselection for signal and background is shown in Figure 4.10.

- The ratio of the transverse momentum of the two SM Higgs bosons,

$$p_T^{\text{ratio}} = \frac{p_T^{\text{LRJ}+\ell}}{p_T^{\text{Di-Tau jet}}}\,, \tag{4.8}$$

gives a measure on the p_T imbalance between the two Higgs bosons in the event. If there is any systematic p_T imbalance, this variable will reflect it. The distribution of p_T^{ratio} after the loose preselection for signal and background is shown in Figure 4.11.

- The mass of the Di-Tau jet and the LRJ as well as the invariant mass of the LRJ plus lepton system. The mass of the Di-Tau jet should peak around the Higgs boson mass, while the mass of the LRJ and the LRJ plus lepton system should peak at the W boson or Higgs boson mass, respectively, or at a value greater than the Higgs boson mass, if the W bosons decay fully hadronically. The distribution of the three masses after the loose preselection for signal and background is shown in Figures 4.12 to 4.14. The low signal mass peak in Figure 4.14 at the Higgs mass represents the topology where one of the W bosons decays leptonically, while the flat signal distribution in this Figure represents the topology where the lepton from the τ lepton decay is added to the Higgs boson decaying into two W bosons.

- From the expected topology of the final state, different distances between the objects can be used for signal and background separation. First, the two SM Higgs boson should be produced back-to-back, which can be investigated using the distance $\Delta R\,(\text{LRJ}, \text{Di-Tau jet})$. Also, if the lepton originates from the W boson decay, the distance between the lepton and the LRJ, $\Delta R\,(\text{LRJ}, \ell)$, should be small, while the distance of the lepton to the Di-Tau jet, $\Delta R\,(\text{Di-Tau jet}, \ell)$, should be large. The distributions of these distances are shown in Figures 4.15 to 4.17.

Before searching for the optimal set of cuts on the above variables, the optimization investigates the optimal WPs for the Di-Tau jet and the veto of b-jets, the latter suppressing backgrounds including t-quarks. The distribution of the Di-Tau jet ID score is shown in Figure 4.18.

The distribution of the signal and background events after tight preselection for all the above variables can be found in Figures B.1 to B.12 in the appendix.

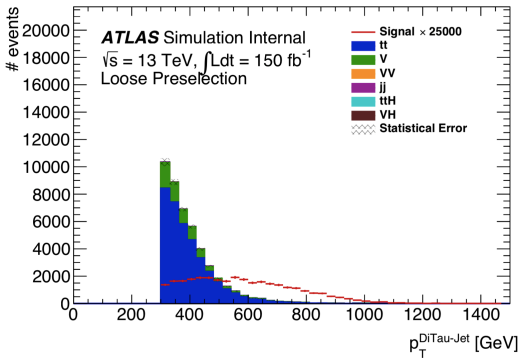

Figure 4.6.: Comparison of the signal and background distribution of $p_T^{\text{Di-Tau jet}}$ after loose preselection.

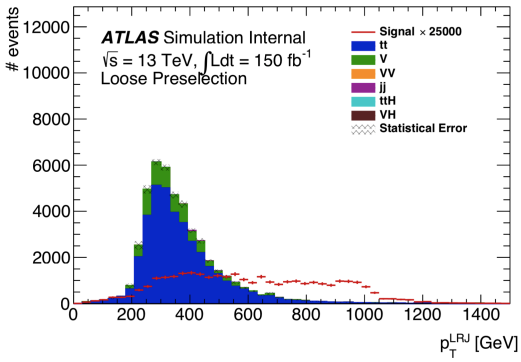

Figure 4.7.: Comparison of the signal and background distribution of p_T^{LRJ} after loose preselection.

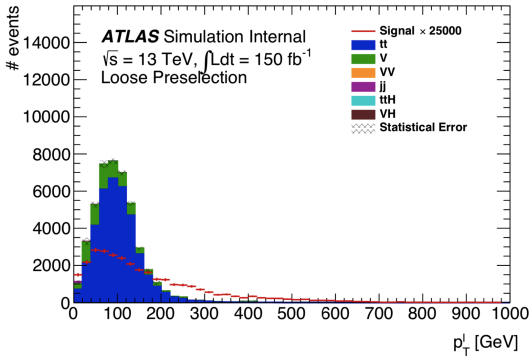

Figure 4.8.: Comparison of the signal and background distribution of p_T^{ℓ} after loose preselection.

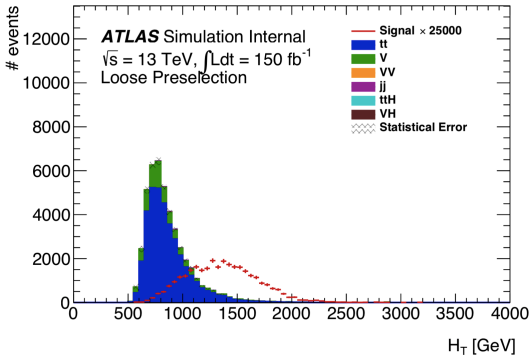

Figure 4.9.: Comparison of the signal and background distribution of H_T after loose preselection.

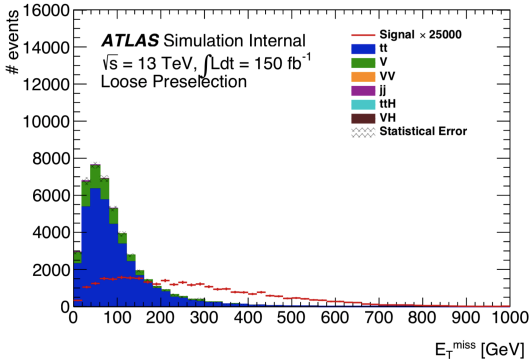

Figure 4.10.: Comparison of the signal and background distribution of E_T^{miss} after loose preselection.

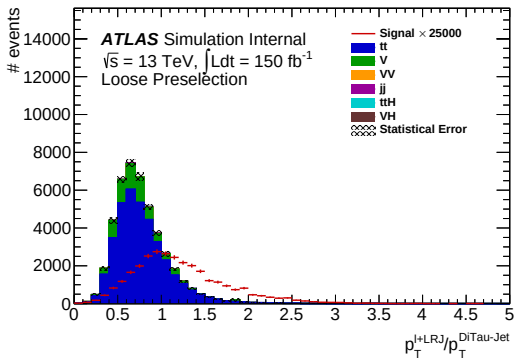

Figure 4.11.: Comparison of the signal and background distribution of p_T^{ratio} after loose preselection.

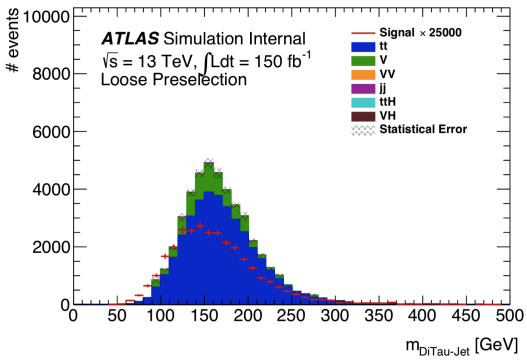

Figure 4.12.: Comparison of the signal and background distribution of $m_{\text{Di-Tau jet}}$ after loose preselection.

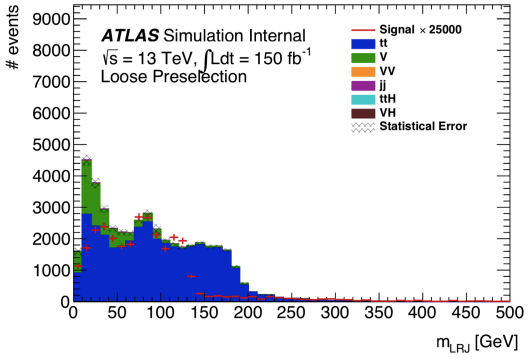

Figure 4.13.: Comparison of the signal and background distribution of m_{LRJ} after loose preselection.

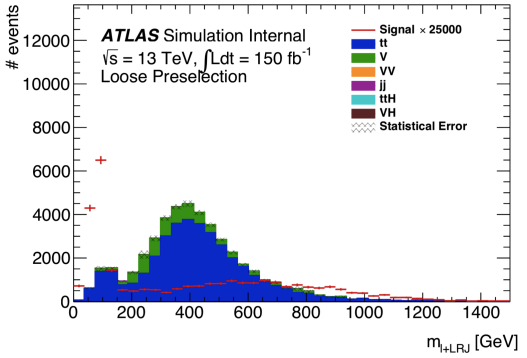

Figure 4.14.: Comparison of the signal and background distribution of $m_{\text{LRJ}+\ell}$ after loose preselection.

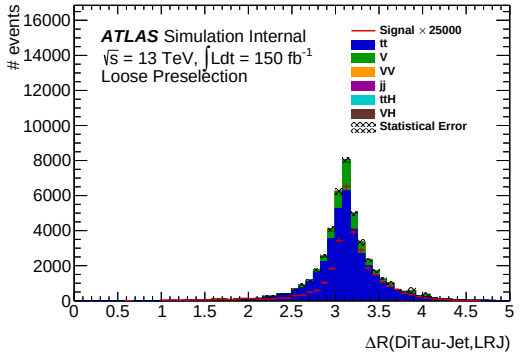

Figure 4.15.: Comparison of the signal and background distribution of $\Delta R\,(\text{Di-Tau jet, LRJ})$ after loose preselection.

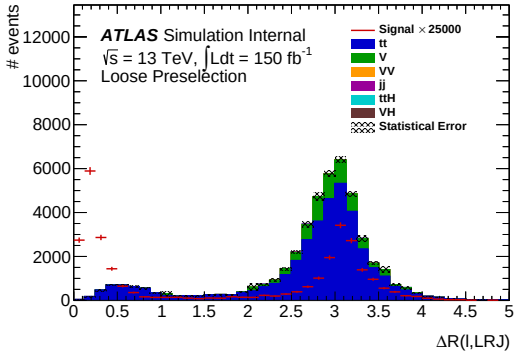

Figure 4.16.: Comparison of the signal and background distribution of $\Delta R\,(\text{LRJ}, \ell)$ after loose preselection.

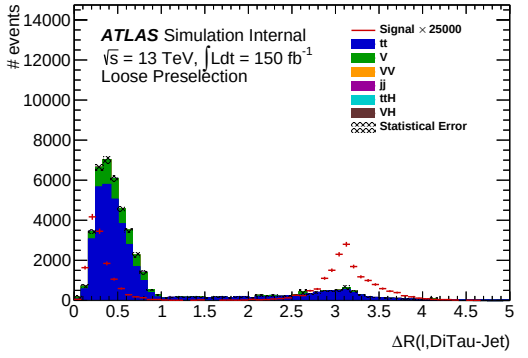

Figure 4.17.: Comparison of the signal and background distribution of $\Delta R\,(\text{Di-Tau jet}, \ell)$ after loose preselection.

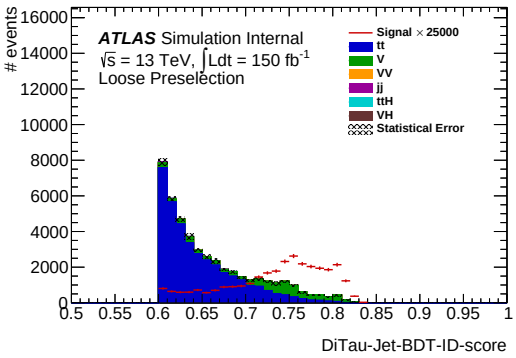

Figure 4.18.: Comparison of the signal and background distribution of the Di-Tau jet ID score after loose preselection.

4.9. Optimization of the Event Selection

Despite the fact that the signal topology already provides a good separation between signal and background events, the preselection does not yield sufficient significance for the observation of the channel, nor a sufficient signal over background ratio. A higher degree of separation can be reached by applying cuts on kinematic variables or distances between the selected objects. In this analysis, the Asimov significance [103]

$$\Sigma_A = \sqrt{2 \times \left((s+b) \ln\left(1 + \frac{s}{b}\right) - s \right)} \tag{4.9}$$

is used to find the optimal set of cuts. Here, s is the number of signal events after all applied cuts, while b is the number of background events after all applied cuts. The Asimov significance is found to be robust in regions with low event yields. The uncertainty on the Asimov significance can be calculated using standard Gaussian error propagation, as the signal and background yield are uncorrelated. This yields

$$\sigma_\Sigma = \Sigma^{-1} \times \sqrt{\left(\ln\left(1 + \frac{s}{b}\right) \times \sigma_s\right)^2 + \left(\left(\ln\left(1 + \frac{s}{b}\right) - \frac{s}{b}\right) \times \sigma_b\right)^2}\,, \tag{4.10}$$

where

$$\sigma_b = \sqrt{\sigma^2_{N_{t\bar{t}}} + \sigma^2_{N_{t\bar{t}H}} + \sigma^2_{N_V} + \sigma^2_{N_{VV}} + \sigma^2_{N_{VH}} + \sigma^2_{N_{jj}}}\,. \tag{4.11}$$

To find the optimal cut, the Asimov significance is determined for different cut values for each variable considered. The best cut values are compared between all variables, and thus the global optimal cut value is found.

However, when conducting the analysis, it became apparent that the amount of MC

events generated for the $t\bar{t}$ and the single boson backgrounds is not sufficient to provide a statistically significant estimate of the expected number of events at an integrated luminosity of $150\,\mathrm{fb}^{-1}$. The amount of generated single boson events is significantly scaled up to match the expected number of events in data, while the amount of generated $t\bar{t}$ events is about the same as the expected number of events in data. This means that one generated event is reweighed to represent one or multiple weighted events, leading to large statistical uncertainties on the weighted events. The problem especially becomes relevant when only few events are left after applying a set of cuts, as the background prediction for $t\bar{t}$ and single bosons will then be dominated by statistical uncertainties and no meaningful statement can be made. For this reason, the shape of the $t\bar{t}$ and single boson background is transferred to the signal region (SR) from a region which is defined by looser cuts than the SR. This looser selection region (LSR) includes more background events, and is thus more reliable. The yield of the $t\bar{t}$ and single boson background is then calculated from the shape of the background in the LSR scaled to the number of events in the SR. The exact use and application of this method is discussed in the next section.

Using a LSR for Background Estimates

As mentioned above, the number of generated background events for the $t\bar{t}$ and single boson background is not sufficient in order to allow for a significant statement on how these backgrounds behave given an optimal set of cuts. Therefore, a LSR region will be used in order to evaluate the shape of these distributions in the SR.

Essentially, the LSR is a region which is defined with a looser set of cuts in order to enhance the event yield. The looser set of cuts consists of the loose preselection and all optimization cuts. Specifically, the tighter Di-Tau jet ID criterion and the b-veto are not applied to the LSR. This is done as the application of the tighter Di-Tau jet ID and the b-veto are assumed to be independent of the kinematic cuts, which preserves the shapes of the distributions. However, because of time constraints, this assumption could not be validated. This is further discussed in Section 6.

The shape of the $t\bar{t}$ and single boson background is then transferred to the SR by taking the distribution in the LSR and weighting it by a factor of

$$w_{\mathrm{LSR}} = \frac{N^{\mathrm{SR}}}{N^{\mathrm{LSR}}}\,, \tag{4.12}$$

where N^{SR} is the number of unweighted MC events in the SR and N^{LSR} is the number of unweighted MC events in the LSR. In a similar way, the number of background events in

the SR can be inferred from the LSR via

$$N^{\mathrm{SR}}_{\mathrm{weighted}} = N^{\mathrm{LSR}}_{\mathrm{weighted}} \times w_{\mathrm{LSR}}\,, \tag{4.13}$$

where $N^{\mathrm{SR}}_{\mathrm{weighted}}$ is the weighted number of events in the SR, $N^{\mathrm{LSR}}_{\mathrm{weighted}}$ is the weighted number of events in the LSR, and w_{LSR} is the weight from Equation 4.12. The uncertainty of the weighted number of events in the SR can be calculated using Gaussian error propagation, i.e.

$$\sigma_{N^{\mathrm{SR}}_{\mathrm{weighted}}} = N^{\mathrm{SR}}_{\mathrm{weighted}} \times \sqrt{\left(\frac{\sigma_{N^{\mathrm{LSR}}_{\mathrm{weighted}}}}{N^{\mathrm{LSR}}_{\mathrm{weighted}}}\right)^2 + \left(\frac{\sigma_{N^{\mathrm{SR}}}}{N^{\mathrm{SR}}}\right)^2 + \left(\frac{\sigma_{N^{\mathrm{LSR}}}}{N^{\mathrm{LSR}}}\right)^2}. \tag{4.14}$$

If the number of unweighted MC events in the SR, N^{SR}, is zero, N^{SR} is artificially set to one, and the uncertainty on N^{SR} is also set to one. This is done in order to take the lack of unweighted MC events into account. If the number of unweighted events in the LSR, N^{LSR}, is zero, $N^{\mathrm{SR}}_{\mathrm{weighted}}$ is artificially set to zero and the uncertainty on $N^{\mathrm{SR}}_{\mathrm{weighted}}$ is set to one. Thus, the backgrounds and their respective uncertainties are slightly overestimated in these cases.

In the following, all distributions and calculations are using the above method for the estimation of the $t\bar{t}$ and single boson background.

Optimized Cutflow

First, the optimal WPs for the Di-Tau jet ID and the b-veto need to be selected. For this, the resulting significance for every possible combination of WPs is investigated. The resulting Asimov significances are shown in Table 4.3. The combination of WPs yielding the highest significance is given by choosing the medium WP for the Di-Tau jet ID and the tight WP for the b-veto. This set of WPs has an Asimov significance of $\Sigma_A = 0.01084(4)$.

The first approach to find the optimal set of cuts after the tight preselection applied two cuts on the distance between signal objects after the preselection. Events are removed, if

$$\Delta R\,(\ell, \mathrm{LRJ}) > 1.5 \quad \text{and} \quad \Delta R\,(\text{Di-Tau jet,LRJ}) < 1.5\,. \tag{4.15}$$

A cut on $\Delta R\,(\ell, \text{Di-Tau jet})$ was not considered, as it is very similar to the application of a cut on $\Delta R\,(\ell, \mathrm{LRJ})$. These cuts are appropriate given the event topology: The Di-Tau jet and the LRJ should be approximately back-to-back, and if the lepton originates from the decay of a W boson, it should be close to the LRJ originating from the decay of the other W boson. Thus, if the investigated topology is the

Di-Tau jet ID WP \ b-veto WP	tight	medium	loose	very loose
very loose	0.00862(2)	0.00909(2)	0.00863(2)	0.004344(10)
loose	0.01016(3)	0.01028(3)	0.00944(3)	0.004589(11)
medium	0.01084(4)	0.01040(4)	0.00922(3)	0.004333(12)
tight	0.00932(5)	0.00880(5)	0.00760(4)	0.003382(13)

Table 4.3.: Asimov significances for all possible combinations of Di-Tau jet ID and b-veto WPs. The number in the brackets is the uncertainty of the last (two last) digits. The combination of a medium Di-Tau ID WP with a tight b-veto yields the highest significance.

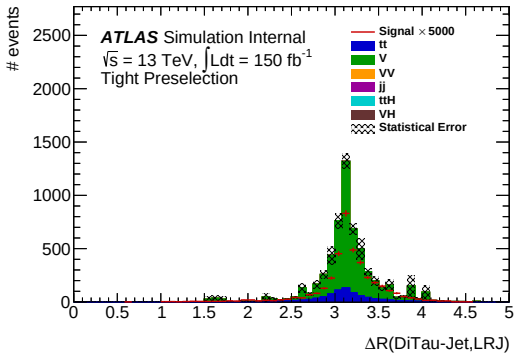

Figure 4.19.: Comparison of the signal and background distribution of $\Delta R\,(\text{Di-Tau jet, LRJ})$ after tight preselection.

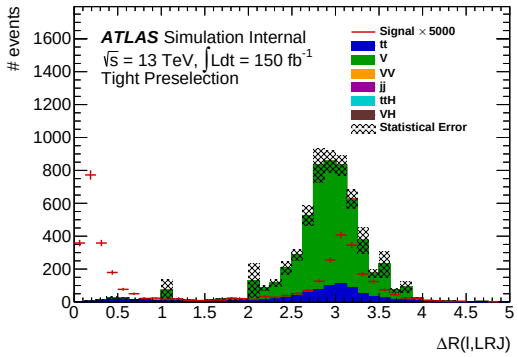

Figure 4.20.: Comparison of the signal and background distribution of $\Delta R\,(\text{LRJ}, \ell)$ after tight preselection.

$HH \to W_{\text{lep}}W_{\text{had}}\tau_{\text{had}}\tau_{\text{had}}$ topology, these cuts should be applied. Comparing this with the distributions of $\Delta R\,(\text{Di-Tau jet,LRJ})$ and $\Delta R\,(\ell, \text{LRJ})$ after the tight preselection in Figures 4.19 and 4.20, it can be observed that at least the former cut yields a good background suppression. However, if this cut is applied, a large fraction of background events is discarded, such that it renders a further optimization impossible as there are simply not enough background events left to make a statement without being in a region of the distribution where the statistical uncertainty does not dominate the yields. Calculating the Asimov significance of this cut yields $\Sigma_A = 0.048(2)$, keeping 0.378(9) signal and 62(24) background events. As this is not a very high significance, both cuts on the distance from Equation 4.15 are removed, in order to be able to conduct a proper optimization on the set of cuts. This has a consequence on the investigated topology: Instead of only investigating the optimal set of cuts for the topology where the lepton comes from a W boson decay, now the topology where the lepton comes from a τ lepton decay is also considered. All

	Algorithm Choice		Final Choice			
Variable	Cut	Significance	Cut	Significance	N_{sig}	N_{bkgd}
$\Delta R\,(\ell, \text{LRJ})$	< 0.375	0.22(6)	< 1.5	0.080(10)	0.379(9)	23(19)
$m_{\text{LRJ}+\ell}$	$< 112.5\,\text{GeV}$	0.050(5)	$< 200\,\text{GeV}$	0.0255(4)	0.353(9)	290(30)
H_T	$> 1300\,\text{GeV}$	0.0255(4)	$> 1050\,\text{GeV}$	0.0214(2)	0.63(2)	700(100)
$p_T^{\text{Di-Tau jet}}$	$> 600\,\text{GeV}$	0.0201(3)	$> 510\,\text{GeV}$	0.0193(2)	0.464(10)	580(70)
E_T^{miss}	$> 400\,\text{GeV}$	0.040(3)	$> 160\,\text{GeV}$	0.0187(3)	0.503(11)	700(200)
p_T^{LRJ}	$> 780\,\text{GeV}$	0.0273(9)	$> 510\,\text{GeV}$	0.0174(2)	0.442(10)	640(100)
p_T^{ratio}	> 1.8	0.0224(20)	> 1	0.0170(2)	0.466(10)	700(200)

Table 4.4.: Algorithm and final choice for the most significant cut on the optimization variables for the first cut after the tight preselection. The corresponding Asimov significance of the cuts is given, as well as the remaining number of signal and background events after the final cut.

ΔR variables, i.e. $\Delta R\,(\text{Di-Tau jet,LRJ})$, $\Delta R\,(\ell, \text{Di-Tau jet})$, and $\Delta R\,(\ell, \text{LRJ})$, are investigated and used for the cut optimization, and the Asimov significance of every possible cut on these variables is calculated and compared to the cuts on the other variables.

In Table 4.4, the most significant cuts found by the optimization algorithm and the most significant final cuts after tight preselection are shown. The optimal cut value found by the algorithm always uses the tails of the signal or background distribution and is therefore replaced by a looser but sensible cut which is chosen manually. This ensures that the cut decision is not driven by statistical fluctuations in the variable distributions. The cut on the signal topology using the distance $\Delta R\,(\ell, \text{LRJ})$ yields the highest significance. However, as discussed previously, it is not possible to further optimize the selection of cuts after applying this cut. The reason is that too few unweighted background events remain in order to make a statement on the significance of the subsequent cut which is not dominated by statistical uncertainties in the background distribution. Therefore, to get a higher total significance after further optimization, the second and third most significant cut are investigated. The distribution of $m_{\text{LRJ}+\ell}$ is shown in Figure 4.21, and the distribution of H_T is shown in Figure 4.22. Also, for both variables the optimal cut is shown.

In a second iteration, the subsequent best cut after the application of one of the above cuts is searched. For this, both the cuts on $m_{\text{LRJ}+\ell}$ and H_T are investigated. The respective cut is applied, and the Asimov significance is calculated for all subsequent cuts which are still sensible to be applied. The Asimov significance for both the algorithm and the final cuts and the signal and background yields for the final cut choice are shown in Table 4.5. For both investigated first cuts, the respective other cut which was applied to the tight preselection distributions is found to be the most significant cut. This optimal

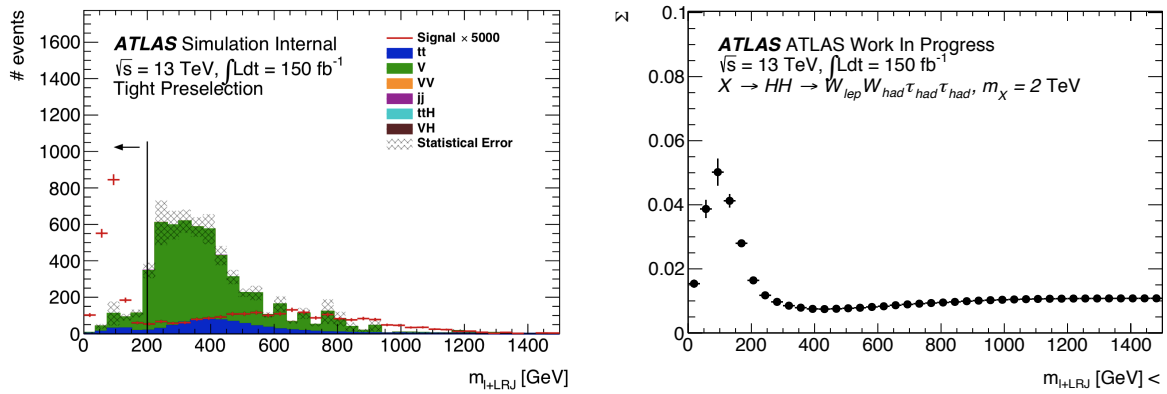

(a) *(b)*

Figure 4.21.: Distribution of (a) $m_{\mathrm{LRJ}+\ell}$ and (b) the Asimov significance of cuts on this distribution after the tight preselection. The solid line indicates the best cut value, where the arrow points towards the region which is kept by the cut.

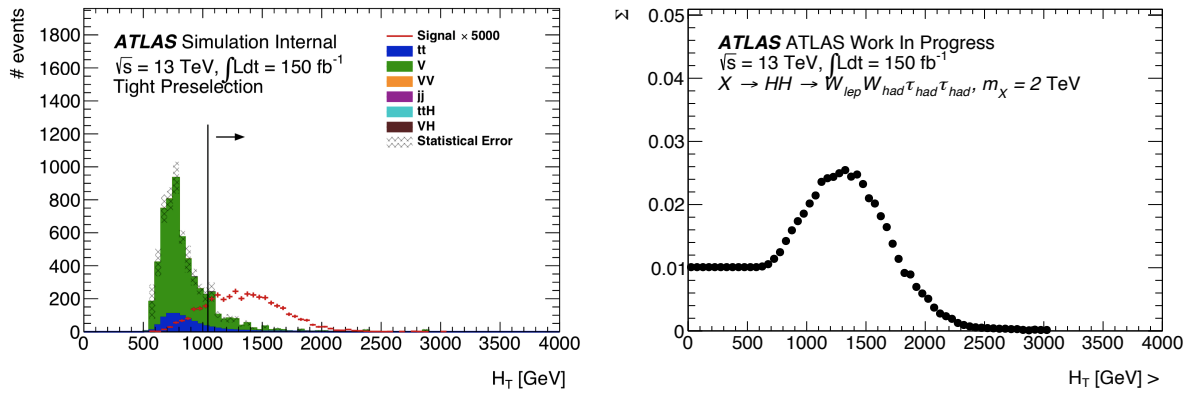

(a) *(b)*

Figure 4.22.: Distribution of (a) H_T and (b) the Asimov significance of cuts on this distribution after the tight preselection. The solid line indicates the best cut value, where the arrow points towards the region which is kept by the cut.

First Cut	Second Cut						
	Variable	Algorithm Choice		Final Choice			
		Cut	Significance	Cut	Significance	N_{sig}	N_{bkgd}
$m_{\text{LRJ}+\ell}$	H_T	$> 1500\,\text{GeV}$	0.4(8.0)	$> 1050\,\text{GeV}$	0.23(6)	0.263(8)	1.3(1.3)
$< 200\,\text{GeV}$	$p_T^{\text{Di-Tau jet}}$	$> 810\,\text{GeV}$	0.3(8.0)	$> 510\,\text{GeV}$	0.104(12)	0.233(7)	5(4)
	E_T^{miss}	$> 320\,\text{GeV}$	0.5(18.0)	$> 140\,\text{GeV}$	0.034(2)	0.222(7)	40(30)
H_T	$m_{\text{LRJ}+\ell}$	$< 112.5\,\text{GeV}$	0.9(10.0)	$< 200\,\text{GeV}$	0.23(6)	0.263(8)	1.3(1.3)
$> 1050\,\text{GeV}$	E_T^{miss}	$> 760\,\text{GeV}$	0.08(2.0)	$> 160\,\text{GeV}$	0.036(2)	0.436(10)	150(50)
	p_T^{ratio}	> 2.9	0.09(3.0)	> 1	0.0303(6)	0.397(9)	170(40)

Table 4.5.: Algorithm and final choice for the most significant cut on the optimization variables for the second cut after the tight preselection. The corresponding Asimov significance of the cuts is given, as well as the remaining number of signal and background events after the final cut.

Cut	Signal	Total Background	Significance Σ_A
Loose Preselection	1.203	44644.4	0.006
Tight Preselection	0.764	5055.54	0.011
$H_T > 1050\,\text{GeV}$	0.63(2)	700(100)	0.0214(2)
$m_{\text{LRJ}+\ell} < 200\,\text{GeV}$	0.263(8)	1.3(1.3)	0.23(6)

Table 4.6.: Expected yields and Asimov significance after application of the optimal set of cuts on $150\,\text{fb}^{-1}$ of data. A more detailed cutflow can be found in Table A.4 in the appendix.

set of cuts has an Asimov significance of

$$\Sigma_A = 0.23(6)\,, \tag{4.16}$$

while keeping 0.263(8) signal and 1.3(1.3) background events, respectively. The distributions of $m_{\text{LRJ}+\ell}$ and H_T with the optimal cuts as well as the significance distributions are shown in Figures 4.23 and 4.24. From these, it is visible that already for these cuts there are only few background events left. However, both cuts are cutting on the edges of distinct shapes of the signal and background distributions, and are therefore considered to be sensible. In the significance plots, the dominance of the statistical uncertainty in regions with low event yields can be seen. After the application of the above set of cuts, no further sensible statement on the next cut can be made, as there are too few events left.

In Table 4.6, a complete cutflow for the optimized selection of cuts can be found. A more detailed cutflow can be found in Table A.4 in the appendix.

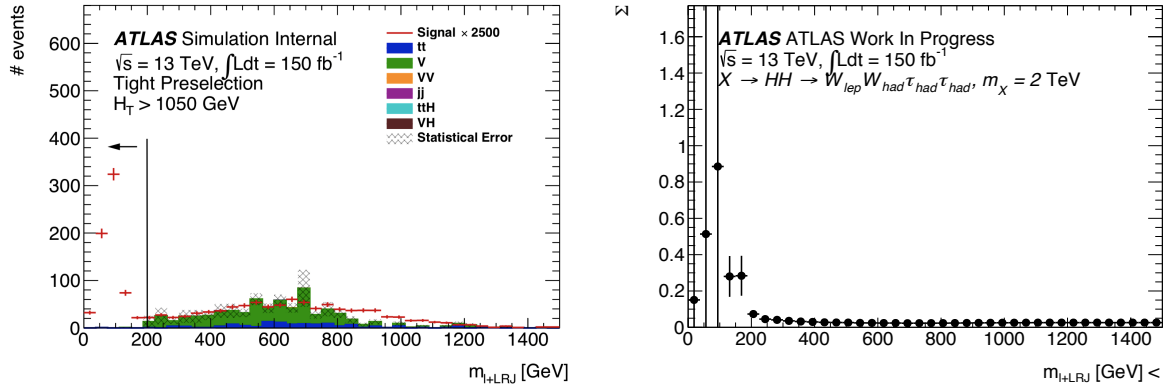

(a) *(b)*

Figure 4.23.: Distribution of (a) $m_{\mathrm{LRJ}+\ell}$ and (b) the Asimov significance of cuts on this distribution after the first optimized cut on H_T. The solid line indicates the best cut value, where the arrow points towards the region which is kept by the cut.

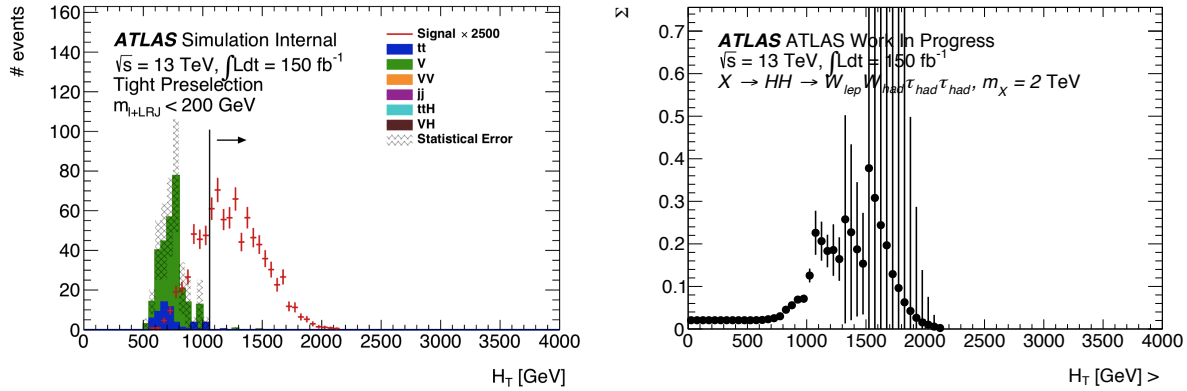

(a) *(b)*

Figure 4.24.: Distribution of (a) H_T and (b) the Asimov significance of cuts on this distribution after the first optimized cut on $m_{\mathrm{LRJ}+\ell}$. The solid line indicates the best cut value, where the arrow points towards the region which is kept by the cut.

5. Statistical Interpretation

In this chapter, the expected exclusion limits on $\sigma_{pp\to X\to HH} \times \mathcal{BR}_{HH\to WW\tau\tau}$ set by the conducted analysis are discussed. The expected limits are calculated taking only statistical uncertainties into account. Due to time constraints, it was not possible to calculate the expected limits including systematic uncertainties on the analysis. However, in a second step an overall systematic uncertainty is assumed and the expected limits are recalculated including both the statistical and this assumed systematic uncertainty.

5.1. Limits with Statistical Uncertainties

The expected yields for the signal process $pp \to X \to HH \to WW\tau\tau \to \geq 1\ell$ with an assumed cross section of $\sigma_{pp\to X\to HH} = 10\,\text{fb}$ and all background processes in $150\,\text{fb}^{-1}$ of data after applying the optimized selection of cuts are shown in Table 5.1. For the signal, 0.263 ± 0.008 events are expected, while for the background, 1.3 ± 1.3 events are expected. The dominant background are single boson events, which make up about 70% of the background, followed by $t\bar{t}$ events with a share of about 23%. The other processes make up 7% of the total background and are approximately negligible compared to the two dominating ones. The Asimov significance of the yields is 0.23 ± 0.06. Thus, the expected signal yield is still consistent with the background only hypothesis. For this reason, expected upper CL_s limits [104] on the cross section are estimated.

The CL_s method for setting upper limits was developed at the LEP collider experiment. It is designed to avoid the spurious exclusions for samples with a low event rate. The

Process	Signal	VH	VV	V	jj	$t\bar{t}$	$t\bar{t}H$	$\sum_{\text{background}}$
Yield	0.263	0	0.051	0.9	0.012	0.3	0	1.3
Uncertainty	±0.008	±1	±0.013	±0.8	±0.008	±0.5	±1	±1.3

Table 5.1.: Expected yields for the signal and all background categories after optimization for an integrated luminosity of $\int \mathcal{L}\text{d}t = 150\,\text{fb}^{-1}$. For the signal, a cross section of 10 fb is assumed, while the background cross sections are according to SM predictions. $\sum_{\text{background}}$ is the sum of all backgrounds. The complete cutflow can be found in Table A.4 in the appendix.

method first simultaneously performs two tests to then calculate the actual limits. If $X(\theta)$ is a sample containing random events created from a probability distribution with a real non-negative parameter θ, and if $1-\alpha'$ is the associated confidence interval, the method tests the hypothesis $H_0 : \theta = \theta_0$ versus the background-only hypothesis $H_1 : \theta = 0$ by calculating

$$\frac{\mathcal{P}\left(\theta_{\text{up}}\left(X\right) < \theta|\theta_0\right)}{\mathcal{P}\left(\theta_{\text{up}}\left(X\right) < \theta|0\right)} \leq \alpha' \tag{5.1}$$

for all θ. $\mathcal{P}$ is the likelihood function based on the event yields. While the numerator describes the probability α of erroneously detecting a nonexistent effect (type-I error), the denominator describes the statistical power $1-\beta$ of the test. β is the probability of the failure to detect an existing effect (type-II error). In conclusion, H_0 is rejected, when the ratio is indeed $\leq \alpha'$.

In the second step, the actual expected limits are calculated. A test statistic $q_\theta\left(X\right)$ is created from the input yields, and the value of θ for which

$$\frac{\mathcal{P}\left(q_\theta\left(X\right) < q_\theta^\star|\theta\right)}{\mathcal{P}\left(q_\theta\left(X\right) < q_\theta^\star|0\right)} = \alpha' \tag{5.2}$$

holds is searched. Here, $q_\theta^\star$ is the expected outcome of the experiment. $q_\theta^\star$ is provided from an Asimov data set providing the median experimental sensitivity corresponding to the yields from Table 5.1 [103].

In this analysis, the software framework HistFactory is used to set expected upper limits at the $1-\alpha' = 95\%$ confidence level. HistFactory is able to take statistical and systematic uncertainties into account and uses these to calculate one and two σ uncertainty bands, where σ is the standard deviation.

The limits and the according error bands are shown in Table 5.2. The expected limit for the signal cross section is $\sigma_{pp\to X\to HH} = 155^{+69}_{-43}\,\text{fb}$. This corresponds to 15.5 times the assumed signal cross section of $\sigma_{\text{signal}} = 10\,\text{fb}$, which was the limit on $\sigma_{pp\to X\to HH}$ set by the $HH \to b\bar{b}b\bar{b}$ analysis.

5.2. Limits with Statistical and Assumed Systematic Uncertainties

Due to time constraints, it was not possible to include any evaluation on systematic uncertainties in this thesis. However, this section discusses the main systematic uncertainties which would be needed to be considered in an evaluation, and gives an estimate on how

	σ / fb	$\mu = \sigma/\sigma_{\text{signal}}$
$+2\sigma$	339	33.9
$+1\sigma$	224	22.4
Median	155	15.5
-1σ	112	11.2
-2σ	83	8.3

Table 5.2.: Expected upper limits on $\sigma_{pp\to X\to HH}$ in fb and in terms of the assumed signal cross section $\sigma_{\text{signal}} = 10\,\text{fb}$ with statistical uncertainties only.

they would possibly influence the upper limits on the cross section.

The systematic uncertainties can be separated in three general groups: theoretical uncertainties, which are uncertainties on any theoretical prediction used in the analysis, modeling uncertainties, which are uncertainties related to the production of the MC samples and the simulation of the detector response, and analysis uncertainties, resulting from methods and tools used in the analysis.

The theoretical uncertainties mostly include the uncertainties on the calculated SM cross sections, the calculated SM branching ratios, and the PDFs used for the calculation of the ME for the hard scattering process. The modeling uncertainties on the one hand include uncertainties from the simulation of the detector response to the incoming parton shower, and on the other hand actual uncertainties which also occur in the actual experiment. The latter includes uncertainties on trigger efficiencies, uncertainties on the normalizations of the energy measurements in the calorimeters, uncertainties from b-tagging and uncertainties on the measurement of the luminosity. An uncertainty also needs to be applied since using a LSR for the estimation of the $t\bar{t}$ and single boson background kinematic distributions might not yield accurate predictions .

To obtain an idea on how the inclusion of systematic uncertainties influences the upper limits on the cross section, an assumed systematic uncertainty on the signal and background yields is introduced, such that

$$\sigma_{\text{systematic}} = \sqrt{3} \times \sigma_{\text{statistic}} \quad \Rightarrow \quad \sqrt{\sigma^2_{\text{statistic}} + \sigma^2_{\text{systematic}}} = 2 \times \sigma_{\text{statistic}}\,. \tag{5.3}$$

This is just a rough estimate of the actual systematic uncertainty of the analysis, and is not a robust estimate of the systematic uncertainties that would need to be evaluated.

The expected upper limits on the cross section together with the one and two σ uncertainty bands for this assumption are shown in Table 5.3. The upper limit would be $\sigma_{signal} = 161^{+68}_{-45}\,\text{fb}$. Compared to the upper limit on the cross section found using only the statistical uncertainties, the limit is raised by 6 fb or about 4%, which corresponds to

	σ / fb	$\mu = \sigma/\sigma_{\text{signal}}$
$+2\sigma$	345	34.5
$+1\sigma$	229	22.9
Median	161	16.1
-1σ	116	11.6
-2σ	87	8.7

Table 5.3.: Expected upper limits on $\sigma_{pp\to X\to HH}$ in fb and in terms of the assumed signal cross section $\sigma_{\text{signal}} = 10\,\text{fb}$ with combined statistical and assumed systematic uncertainties.

a rise of less than $0.1\,\sigma$ for the expected limit using only statistical uncertainties.

6. Conclusion and Outlook

In this thesis, the ATLAS sensitivity to the new $X \rightarrow HH \rightarrow WW\tau\tau \rightarrow 1\ell +$ jets channel in the boosted topology where X is a heavy CP even scalar resonance from a 2HDM was estimated.

To simulate signal events, a total of 14 samples in LO and NLO were produced, corresponding to seven different heavy resonant mass points. For the official production, a LO sample with a heavy resonant mass of $m_X = 2\,\text{TeV}$ was requested. The used JOs for ATLAS MC production were thoroughly validated. It is shown that the wanted processes and signatures are indeed present in the produced samples. Also, the kinematic distributions of the signal process were shown to indeed exhibit a boosted topology, justifying the use of a boosted analysis strategy.

The shape comparison between the distributions of the LO and NLO sample at a mass point of $m_X = 1\,\text{TeV}$ shows no inconsistency. It would thus be justified to use NLO samples generated in the presented way for any upcoming analysis, given the needed computing resources are available.

The boosted topology allowed for a good background suppression, however, it also came with challenges. This especially concerned the OLR and the handling of Di-Tau jets and LRJs. An optimized set of cuts for the analysis was presented. It isolated the boosted signature with one lepton originating from the decay of a W boson. The signature where the lepton originates from a τ lepton decay is suppressed by the optimal set of cuts. The optimal set of cuts yielding the highest Asimov significance was

- $H_T > 1050\,\text{GeV}$
- $m_{\text{LRJ}+\ell} < 200\,\text{GeV}$

with a maximum Asimov significance of $\Sigma_A = 0.23 \pm 0.06$. The expected event yields for the signal and background in $150\,\text{fb}^{-1}$ of data and an assumed signal cross section of $\sigma_{\text{signal}} = 10\,\text{fb}$ were found to be

$$N_{\text{signal}} = 0.263 \pm 0.008 \quad \text{and}$$
$$N_{\text{background}} = 1.3 \pm 1.3\,.$$

The luminosity approximately matches the amount of data collected by ATLAS at the end of Run 2, and the assumed cross section is the upper limit on the cross section found by the $HH \to b\bar{b}b\bar{b}$ analysis. An upper limit on the cross section using statistical uncertainties only was found to be $\sigma_{pp\to X\to HH} = 155^{+69}_{-43}\,\text{fb}$, corresponding to 15.5 times the assumed signal cross section. An upper limit on the cross section using statistical as well as assumed systematic uncertainties yielded a slightly higher value of $\sigma_{pp\to X\to HH} = 161^{+68}_{-45}\,\text{fb}$. This limit is about 16 times the limit found by the $HH \to b\bar{b}b\bar{b}$ analysis which is in contrast to this analysis not limited by the amount of generated MC events. Thus, even if the limits found in this analysis are not compatible with the limits found by the $HH \to b\bar{b}b\bar{b}$ analysis, they are still quite promising. However, for the channel to significantly contribute to cross section measurement, the amount of collected data needs to be larger.

The analysis was mostly constrained by two major issues: The amount of generated MC events available for the background estimation, and time to include additional tools and methods and to evaluate and improve the analysis choices. The number of generated MC events for the background estimation could be improved by including the recently produced MC16e samples, exhibiting the pile-up profile for the 2018 data taking. To improve the number of generated MC events for the $t\bar{t}$ and single boson background, the samples produced using the Sherpa MC event generator could be used for the analysis, as they contain more events than the used PowhegPythia and Pythia samples, respectively. This would render using the LSR for the estimation of these two background contributions obsolete, removing a systematic uncertainty from the analysis. Also, with more generated MC events available, a multivariate analysis could possibly be conducted.

On the analysis level, an improved analysis should include or improve several aspects over the current version of the analysis. The selection of the Di-Tau jet used in the analysis using the Di-Tau jet with the highest BDT ID score is very prone to modeling issues in the high BDT ID score region. It would be better to choose the Di-Tau jet e.g. via a criterion on the transverse momentum p_T, or via first selecting the LRJ originating from the W boson decay and imposing a ΔR condition to find the matching Di-Tau jet. In addition, merging the different trigger conditions via a logical "OR" condition might yield problems in estimating the systematic uncertainties on the trigger efficiencies. However, this problem could be resolved quite easily by only using one trigger per event. Also, the inclusion of track assisted variables for e.g. the calculation of jet masses would be beneficial, as they provide a better jet mass resolution.

The OLR between leptons, especially electrons, and Di-Tau jets should be reevaluated, as there was no time to check how efficient the used OLR actually is, and if there is a better possible OLR between these objects. The object selection should be reoptimized

for the use with the $WW\tau\tau \rightarrow \geq 1\ell$ topology instead of the $W_{\text{lep}}W_{\text{had}}\tau_{\text{had}}\tau_{\text{had}}$ topology. The current selection favors $W_{\text{had}}W_{\text{had}}\tau_{\text{lep}}\tau_{\text{had}}$ events containing electrons, as at least two subjets are required in the Di-Tau jet and electrons are more likely to fake jet originating from a hadronic τ lepton decay than muons.

Finally, further weights on the generated MC events should be included, in order to better reflect the actually observed distributions in the MC estimate. This includes the scale factors on the different objects as well as the pile-up and vertex weights, as mentioned in Section 4.4.

In the estimation of uncertainties, the systematic uncertainties should be included. This would be useful in order to make a statement on whether the analysis is more limited by statistical or by systematic constraints. Especially, this concerns the uncertainty on the estimation of the $t\bar{t}$ and single boson backgrounds using the LSR, but of course also all the other uncertainties mentioned in Section 5.2.

Despite all these possible improvements, the analysis gives a reasonable estimate on the ATLAS sensitivity to the boosted $pp \rightarrow X \rightarrow HH \rightarrow WW\tau\tau \rightarrow \geq 1\ell$ final state. The results can possibly be combined with other subchannels, such as the investigation of the non-resonant $HH \rightarrow WW\tau\tau$ final state.

A. Additional Tables

This chapter contains additional tables including additional and more detailed information on the analysis.

A.1. MC Samples

In this section, the full list of used background samples is given. The used samples from the MC16a and MC16d production campaign are shown in Table A.1 and A.2, respectively. The used cross sections, branching ratios and filter efficiencies as well as the number of generated events is shown in Table A.3.

Process	Subprocess	Sample name
V	$W^+ \to e\nu$	mc16_13TeV.361100.PowhegPythia8EvtGen_AZNLOCTEQ6L1_ Wplusenu.merge.AOD.e3601_s3126_r9364_r9315
	$W^+ \to \mu\nu$	mc16_13TeV.361101.PowhegPythia8EvtGen_AZNLOCTEQ6L1_ Wplusmunu.merge.AOD.e3601_s3126_r9364_r9315
	$W^+ \to \tau\nu$	mc16_13TeV.361102.PowhegPythia8EvtGen_AZNLOCTEQ6L1_ Wplustaunu.merge.AOD.e3601_s3126_r9364_r9315
	$W^- \to e\nu$	mc16_13TeV.361103.PowhegPythia8EvtGen_AZNLOCTEQ6L1_ Wminusenu.merge.AOD.e3601_s3126_r9364_r9315
	$W^- \to \mu\nu$	mc16_13TeV.361104.PowhegPythia8EvtGen_AZNLOCTEQ6L1_ Wminusmunu.merge.AOD.e3601_s3126_r9364_r9315
	$W^- \to \tau\nu$	mc16_13TeV.361105.PowhegPythia8EvtGen_AZNLOCTEQ6L1_ Wminustaunu.merge.AOD.e3601_s3126_r9364_r9315
	$Z \to ee$	mc16_13TeV.361106.PowhegPythia8EvtGen_AZNLOCTEQ6L1_ Zee.merge.AOD.e3601_s3126_r9364_r9315
	$Z \to \mu\mu$	mc16_13TeV.361107.PowhegPythia8EvtGen_AZNLOCTEQ6L1_ Zmumu.merge.AOD.e3601_s3126_r9364_r9315
	$Z \to \tau\tau$	mc16_13TeV.361108.PowhegPythia8EvtGen_AZNLOCTEQ6L1_ Ztautau.merge.AOD.e3601_s3126_r9364_r9315

Continued on next page

Table A.1 – continued from previous page

Process	Subprocess	Sample name
VV	$WW \to \ell\nu\ell\nu$	mc16_13TeV.361600.PowhegPy8EG_CT10nloME_AZNLOCTEQ6L1_WWlvlv.merge.AOD.e4616_s3126_r9364_r9315
	$WW \to \ell\nu qq$	mc16_13TeV.361606.PowhegPy8EG_CT10nloME_AZNLOCTEQ6L1_WWlvqq.merge.AOD.e4711_s3126_r9364_r9315
	$WZ \to \ell\nu\ell\ell$	mc16_13TeV.361601.PowhegPy8EG_CT10nloME_AZNLOCTEQ6L1_WZlvll_mll4.merge.AOD.e4475_s3126_r9364_r9315
	$WZ \to \ell\nu\nu\nu$	mc16_13TeV.361602.PowhegPy8EG_CT10nloME_AZNLOCTEQ6L1_WZlvvv_mll4.merge.AOD.e4054_s3126_r9364_r9315
	$WZ \to qq\ell\ell$	mc16_13TeV.361607.PowhegPy8EG_CT10nloME_AZNLOCTEQ6L1_WZqqll_mll20.merge.AOD.e4711_s3126_r9364_r9315
	$WZ \to \ell\nu qq$	mc16_13TeV.361609.PowhegPy8EG_CT10nloME_AZNLOCTEQ6L1_WZlvqq_mqq20.merge.AOD.e4711_s3126_r9364_r9315
	$ZZ \to \ell\ell\ell\ell$	mc16_13TeV.361603.PowhegPy8EG_CT10nloME_AZNLOCTEQ6L1_ZZllll_mll4.merge.AOD.e4475_s3126_r9364_r9315
	$ZZ \to \nu\nu\ell\ell$	mc16_13TeV.361604.PowhegPy8EG_CT10nloME_AZNLOCTEQ6L1_ZZvvll_mll4.merge.AOD.e4475_s3126_r9364_r9315
	$ZZ \to \nu\nu\nu\nu$	mc16_13TeV.361605.PowhegPy8EG_CT10nloME_AZNLOCTEQ6L1_ZZvvvv_mll4.merge.AOD.e4054_s3126_s3136_r9364_r9315
	$ZZ \to qq\ell\ell$	mc16_13TeV.361610.PowhegPy8EG_CT10nloME_AZNLOCTEQ6L1_ZZqqll_mqq20mll20.merge.AOD.e4711_s3126_r9364_r9315
VH	WH	mc16_13TeV.342284.Pythia8EvtGen_A14NNPDF23LO_WH125_inc.merge.AOD.e4246_s3126_r9364_r9315

Continued on next page

Table A.1 – continued from previous page

Process	Subprocess	Sample name
	ZH	mc16_13TeV.342285.Pythia8EvtGen_A14NNPDF23LO_ZH125_inc.merge.AOD.e4246_s3126_r9364_r9315
jj	$jj2$	mc16_13TeV.361022.Pythia8EvtGen_A14NNPDF23LO_jetjet_JZ2W.merge.AOD.e3668_s3126_r9364_r9315
	$jj3$	mc16_13TeV.361023.Pythia8EvtGen_A14NNPDF23LO_jetjet_JZ3W.merge.AOD.e3668_s3126_r9364_r9315
	$jj4$	mc16_13TeV.361024.Pythia8EvtGen_A14NNPDF23LO_jetjet_JZ4W.merge.AOD.e3668_s3126_r9364_r9315
	$jj5$	mc16_13TeV.361025.Pythia8EvtGen_A14NNPDF23LO_jetjet_JZ5W.merge.AOD.e3668_s3126_r9364_r9315
	$jj6$	mc16_13TeV.361026.Pythia8EvtGen_A14NNPDF23LO_jetjet_JZ6W.merge.AOD.e3569_s3126_r9364_r9315
	$jj7$	mc16_13TeV.361027.Pythia8EvtGen_A14NNPDF23LO_jetjet_JZ7W.merge.AOD.e3668_s3126_r9364_r9315
	$jj8$	mc16_13TeV.361028.Pythia8EvtGen_A14NNPDF23LO_jetjet_JZ8W.merge.AOD.e3569_s3126_r9364_r9315
	$jj9$	mc16_13TeV.361029.Pythia8EvtGen_A14NNPDF23LO_jetjet_JZ9W.merge.AOD.e3569_s3126_r9364_r9315
	$jj10$	mc16_13TeV.361030.Pythia8EvtGen_A14NNPDF23LO_jetjet_JZ10W.merge.AOD.e3569_s3126_r9364_r9315
	$jj11$	mc16_13TeV.361031.Pythia8EvtGen_A14NNPDF23LO_jetjet_JZ11W.merge.AOD.e3569_s3126_r9364_r9315
	$jj12$	mc16_13TeV.361032.Pythia8EvtGen_A14NNPDF23LO_jetjet_JZ12W.merge.AOD.e3668_s3126_s3136_r9364_r9315
$t\bar{t}$	–	mc16_13TeV.410470.PhPy8EG_A14_ttbar_hdamp258p75_nonallhad.merge.AOD.e6337_e5984_s3126_r9364_r9315
$t\bar{t}H$	–	mc16_13TeV.343366.aMcAtNloPythia8EvtGen_A14_NNPDF23_NNPDF30ME_ttH125_semilep.merge.AOD.e4706_e5984_s3126_r9364_r9315

Table A.1.: Generated MC samples using the MC16a pile-up profile used for the background estimation.

Continued on next page

Table A.1 – continued from previous page

Process	Subprocess	Sample name
V	$W^+ \to e\nu$	mc16_13TeV.361100.PowhegPythia8EvtGen_AZNLOCTEQ6L1_Wplusenu.merge.AOD.e3601_s3126_r10201_r10210
	$W^+ \to \mu\nu$	mc16_13TeV.361101.PowhegPythia8EvtGen_AZNLOCTEQ6L1_Wplusmunu.merge.AOD.e3601_s3126_r10201_r10210
	$W^+ \to \tau\nu$	mc16_13TeV.361102.PowhegPythia8EvtGen_AZNLOCTEQ6L1_Wplustaunu.merge.AOD.e3601_s3126_r10201_r10210
	$W^- \to e\nu$	mc16_13TeV.361103.PowhegPythia8EvtGen_AZNLOCTEQ6L1_Wminusenu.merge.AOD.e3601_s3126_r10201_r10210
	$W^- \to \mu\nu$	mc16_13TeV.361104.PowhegPythia8EvtGen_AZNLOCTEQ6L1_Wminusmunu.merge.AOD.e3601_s3126_r10201_r10210
	$W^- \to \tau\nu$	mc16_13TeV.361105.PowhegPythia8EvtGen_AZNLOCTEQ6L1_Wminustaunu.merge.AOD.e3601_s3126_r10201_r10210
	$Z \to ee$	mc16_13TeV.361106.PowhegPythia8EvtGen_AZNLOCTEQ6L1_Zee.merge.AOD.e3601_s3126_r10201_r10210
	$Z \to \mu\mu$	mc16_13TeV.361107.PowhegPythia8EvtGen_AZNLOCTEQ6L1_Zmumu.merge.AOD.e3601_s3126_r10201_r10210
	$Z \to \tau\tau$	mc16_13TeV.361108.PowhegPythia8EvtGen_AZNLOCTEQ6L1_Ztautau.merge.AOD.e3601_s3126_r10201_r10210
VV	$WW \to \ell\nu\ell\nu$	mc16_13TeV.361600.PowhegPy8EG_CT10nloME_AZNLOCTEQ6L1_WWlvlv.merge.AOD.e4616_s3126_r10201_r10210
	$WW \to \ell\nu qq$	mc16_13TeV.361606.PowhegPy8EG_CT10nloME_AZNLOCTEQ6L1_WWlvqq.merge.AOD.e4711_s3126_r10201_r10210
	$WZ \to \ell\nu\ell\ell$	mc16_13TeV.361601.PowhegPy8EG_CT10nloME_AZNLOCTEQ6L1_WZlvll_mll4.merge.AOD.e4475_e5984_s3126_r10201_r10210
	$WZ \to \ell\nu\nu\nu$	mc16_13TeV.361602.PowhegPy8EG_CT10nloME_AZNLOCTEQ6L1_WZlvvv_mll4.merge.AOD.e4054_s3126_r10201_r10210

Continued on next page

Table A.2 – continued from previous page

Process	Subprocess	Sample name
	$WZ \to qq\ell\ell$	mc16_13TeV.361607.PowhegPy8EG_CT10nloME_ AZNLOCTEQ6L1_WZqqll_mll20.merge.AOD.e4711_s3126_ r10201_r10210
	$WZ \to \ell\nu qq$	mc16_13TeV.361609.PowhegPy8EG_CT10nloME_ AZNLOCTEQ6L1_WZlvqq_mqq20.merge.AOD.e4711_s3126_ r10201_r10210
	$ZZ \to \ell\ell\ell\ell$	mc16_13TeV.361603.PowhegPy8EG_CT10nloME_ AZNLOCTEQ6L1_ZZllll_mll4.merge.AOD.e4475_e5984_ s3126_r10201_r10210
	$ZZ \to \nu\nu\ell\ell$	mc16_13TeV.361604.PowhegPy8EG_CT10nloME_ AZNLOCTEQ6L1_ZZvvll_mll4.merge.AOD.e4475_e5984_ s3126_r10201_r10210
	$ZZ \to \nu\nu\nu\nu$	mc16_13TeV.361605.PowhegPy8EG_CT10nloME_ AZNLOCTEQ6L1_ZZvvvv_mll4.merge.AOD.e4054_e5984_ s3126_r10201_r10210
	$ZZ \to qq\ell\ell$	mc16_13TeV.361610.PowhegPy8EG_CT10nloME_ AZNLOCTEQ6L1_ZZqqll_mqq20mll20.merge.AOD.e4711_ s3126_r10201_r10210
VH	WH	mc16_13TeV.342284.Pythia8EvtGen_A14NNPDF23LO_WH125_ inc.merge.AOD.e4246_e5984_s3126_r10201_r10210
	ZH	mc16_13TeV.342285.Pythia8EvtGen_A14NNPDF23LO_ZH125_ inc.merge.AOD.e4246_e5984_s3126_r10201_r10210
jj	$jj2$	mc16_13TeV.361022.Pythia8EvtGen_A14NNPDF23LO_ jetjet_JZ2W.merge.AOD.e3668_s3126_r10201_r10210
	$jj3$	mc16_13TeV.361023.Pythia8EvtGen_A14NNPDF23LO_ jetjet_JZ3W.merge.AOD.e3668_s3126_r10201_r10210
	$jj4$	mc16_13TeV.361024.Pythia8EvtGen_A14NNPDF23LO_ jetjet_JZ4W.merge.AOD.e3668_s3126_r10201_r10210
	$jj5$	mc16_13TeV.361025.Pythia8EvtGen_A14NNPDF23LO_ jetjet_JZ5W.merge.AOD.e3668_s3126_r10201_r10210
	$jj6$	mc16_13TeV.361026.Pythia8EvtGen_A14NNPDF23LO_ jetjet_JZ6W.merge.AOD.e3569_e5984_s3126_r10201_ r10210

Continued on next page

Table A.2 – continued from previous page

Process	Subprocess	Sample name
	$jj7$	mc16_13TeV.361027.Pythia8EvtGen_A14NNPDF23LO_ jetjet_JZ7W.merge.AOD.e3668_s3126_r10201_r10210
	$jj8$	mc16_13TeV.361028.Pythia8EvtGen_A14NNPDF23LO_ jetjet_JZ8W.merge.AOD.e3569_s3126_r10201_r10210
	$jj9$	mc16_13TeV.361029.Pythia8EvtGen_A14NNPDF23LO_ jetjet_JZ9W.merge.AOD.e3569_s3126_r10201_r10210
	$jj10$	mc16_13TeV.361030.Pythia8EvtGen_A14NNPDF23LO_ jetjet_JZ10W.merge.AOD.e3569_s3126_r10201_r10210
	$jj11$	mc16_13TeV.361031.Pythia8EvtGen_A14NNPDF23LO_ jetjet_JZ11W.merge.AOD.e3569_s3126_r10201_r10210
	$jj12$	mc16_13TeV.361032.Pythia8EvtGen_A14NNPDF23LO_ jetjet_JZ12W.merge.AOD.e3668_s3126_r10201_r10210
$t\bar{t}$	–	mc16_13TeV.410470.PhPy8EG_A14_ttbar_hdamp258p75_ nonallhad.merge.AOD.e6337_e5984_s3126_r10201_r10210
$t\bar{t}H$	–	mc16_13TeV.343366.aMcAtNloPythia8EvtGen_A14_ NNPDF23_NNPDF30ME_ttH125_semilep.merge.AOD.e4706_ e5984_s3126_r10201_r10210

Table A.2.: Generated MC samples using the MC16d pile-up profile used for the background estimation.

					# generated events	
Process	Subprocess	σ/ pb	BR	ϵ	MC16a	MC16d
Signal	-	0.01	0.0269	0.2333	20,000	30,000
V	$W^- \to e\nu$	8,529	1	1	49,904,000	49,961,000
	$W^- \to \mu\nu$	8,529	1	1	31,973,000	31,978,000
	$W^- \to \tau\nu$	8,529	1	1	19,955,000	19,970,000
	$W^+ \to e\nu$	11,521	1	1	29,929,000	29,953,000
	$W^+ \to \mu\nu$	11,521	1	1	39,962,000	39,952,000
	$W^+ \to \tau\nu$	11,521	1	1	29,982,000	29,959,000
	$Z \to ee$	1,886	1	1	79,293,000	79,340,000
	$Z \to \mu\mu$	1,886	1	1	79,874,000	80,919,000
	$Z \to \tau\tau$	1,886	1	1	39,495,000	37,114,000
VV	$WW \to \ell\nu\ell\nu$	10.631	1	1	14,770,000	14,956,000
	$WW \to \ell\nu qq$	44.176	1	1	4,369,000	4,400,000

Continued on next page

Table A.3 – continued from previous page

Process	Subprocess	σ/ pb	BR	ϵ	# generated events MC16a	MC16d
	$WZ \to \ell\nu\ell\ell$	4.5023	1	1	10,010,000	10,001,000
	$WZ \to \ell\nu qq$	10.099	1	1	9,769,000	9,728,000
	$WZ \to \ell\nu\nu\nu$	2.7778	1	1	985,000	975,000
	$WZ \to qq\ell\ell$	3.2849	1	1	1,490,000	1,476,000
	$ZZ \to \ell\ell\ell\ell$	1.2673	1	1	3,980,000	3,950,000
	$ZZ \to qq\ell\ell$	2.2739	1	1	3,990,000	3,988,000
	$ZZ \to \nu\nu\ell\ell$	0.91795	1	1	995,000	995,000
	$ZZ \to \nu\nu\nu\nu$	0.54901	1	1	200,000	200,000
VH	WH	1.1	1	1	100,000	100,000
	ZH	0.601	1	1	100,000	100,000
jj	$jj2$	2,433,200,000	1	3.3264×10^{-4}	15,989,500	15,981,000
	$jj3$	26,454,000	1	3.1953×10^{-4}	15,879,500	15,878,500
	$jj4$	254,630	1	5.3009×10^{-4}	15,925,500	15,974,500
	$jj5$	4,553.5	1	9.2325×10^{-4}	15,993,500	15,991,500
	$jj6$	257.53	1	9.4016×10^{-4}	17,834,000	17,880,400
	$jj7$	16.215	1	3.9282×10^{-4}	15,983,000	15,116,500
	$jj8$	0.62502	1	101.62×10^{-4}	15,999,000	15,987,000
	$jj9$	0.019639	1	120.54×10^{-4}	13,995,500	14,511,500
	$jj10$	0.0011962	1	58.935×10^{-4}	13,985,000	15,988,000
	$jj11$	4.23×10^{-5}	1	27.015×10^{-4}	15,948,000	15,993,000
	$jj12$	1.04×10^{-6}	1	4.25×10^{-4}	15,995,600	15,640,000
$t\bar{t}H$	-	0.22276	1	1	4,980,000	5,000,000
$t\bar{t}$	-	831.76	1	0.543	119,432,000	74,486,000

Table A.3.: Summary of the cross sections, branching ratios, and filter efficiencies for all considered processes.

A.2. Optimization

In Table A.4, a complete cutflow is shown for the optimal set of cuts found by the analysis, separated into all background contributions.

Cut \ Process	Signal	VH	VV	V	jj	$t\bar{t}$	$t\bar{t}H$	$\sum_{bkgd}$
Loose Preselection	1.2± 0.02	0.29±0.07	18 ±2	7290±360	242±28	3709±290	0.057±0.002	11260±470
Tight Preselection	0.76 ±0.02	0.08±0.04	5±1	4950±250	5±3	771±6	0.0016±0.0002	5730±250
$H_T > 1050$ GeV	0.63 ±0.02	0.05±0.03	1.6±0.7	580±70	3.3±1.8	108±16	0	690±80
$m_{\mathrm{LRJ}+\ell} < 200$ GeV	0.263±0.008	0	0.051±0.013	0.9±0.8	0.012±0.008	0.3±0.5	0	1.3±1.3

Table A.4.: Detailed optimized cutflow.

B. Additional Figures

This chapter contains additional figures including additional and more detailed information on the analysis.

B.1. Separation Power after Tight Preselection

Additional figures illustrating the separation power of the investigated optimization variables are shown in Figure B.1 to B.12.

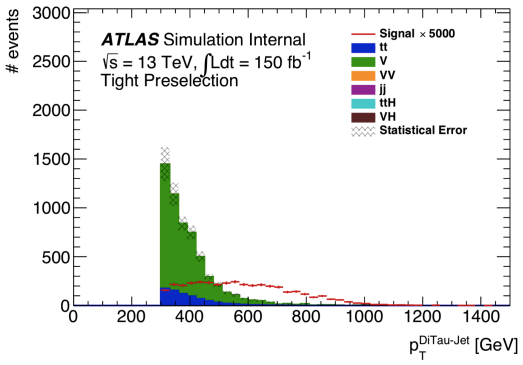

Figure B.1.: Comparison of the signal and background distribution of $p_T^{\text{Di-Tau jet}}$ after tight preselection.

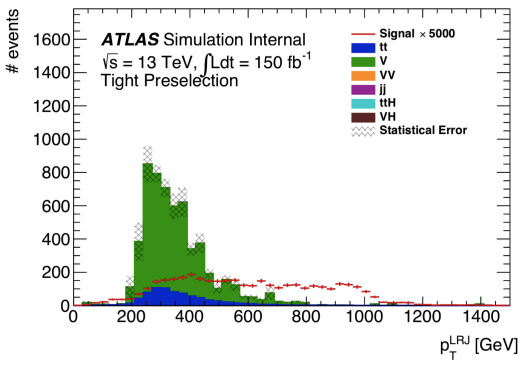

Figure B.2.: Comparison of the signal and background distribution of p_T^{LRJ} after tight preselection.

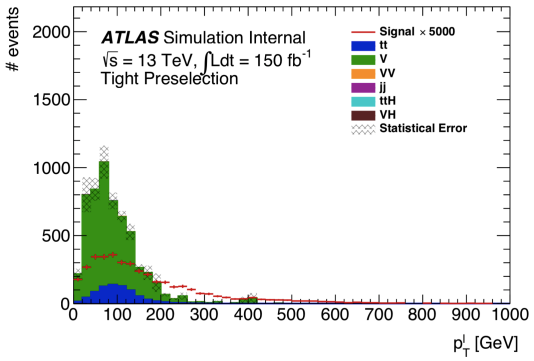

Figure B.3.: Comparison of the signal and background distribution of p_T^ℓ after tight preselection.

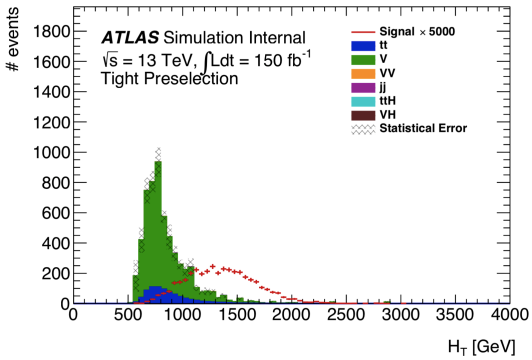

Figure B.4.: Comparison of the signal and background distribution of H_T after tight preselection.

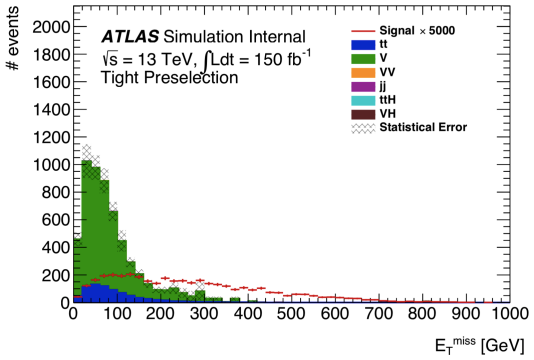

Figure B.5.: Comparison of the signal and background distribution of E_T^{miss} after tight preselection.

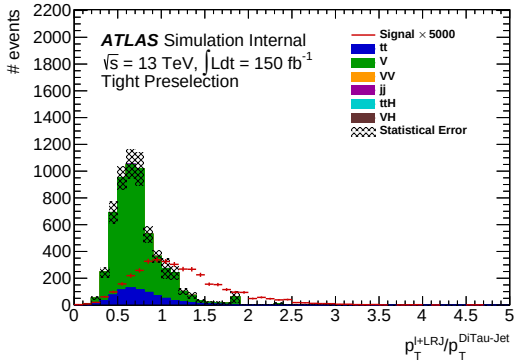

Figure B.6.: Comparison of the signal and background distribution of p_T^{ratio} after tight preselection.

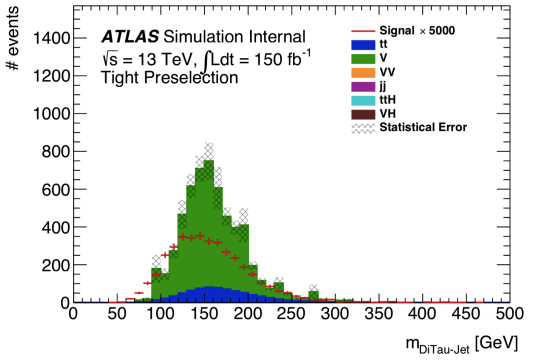

Figure B.7.: Comparison of the signal and background distribution of $m_{\text{Di-Tau jet}}$ after tight preselection.

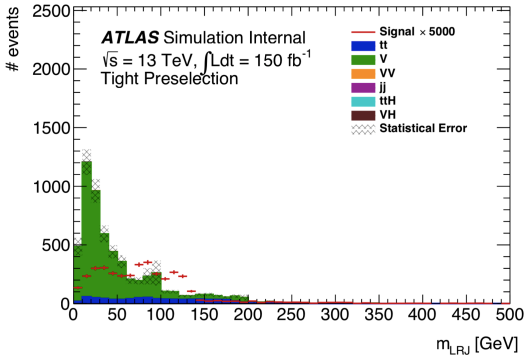

Figure B.8.: Comparison of the signal and background distribution of m_{LRJ} after tight preselection.

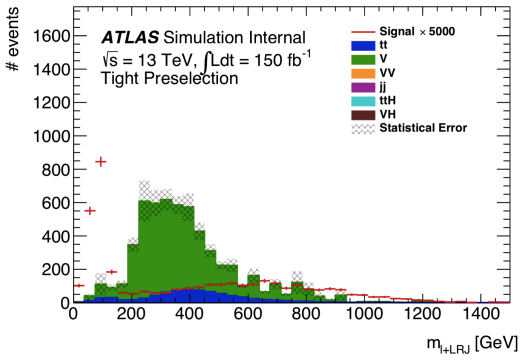

Figure B.9.: Comparison of the signal and background distribution of $m_{\mathrm{LRJ}+\ell}$ after tight preselection.

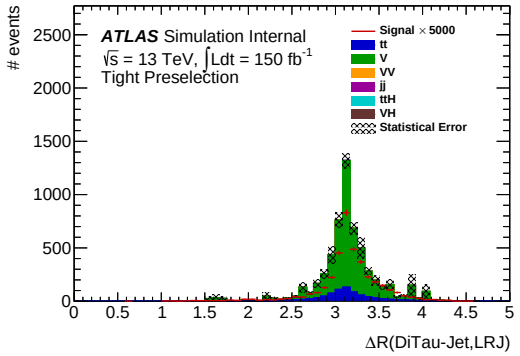

Figure B.10.: Comparison of the signal and background distribution of $\Delta R\,(\text{Di-Tau jet, LRJ})$ after tight preselection.

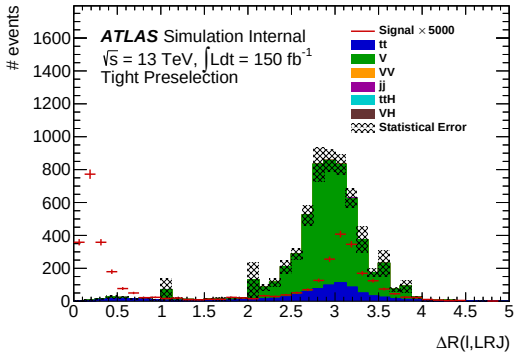

Figure B.11.: Comparison of the signal and background distribution of $\Delta R\,(\mathrm{LRJ}, \ell)$ after tight preselection.

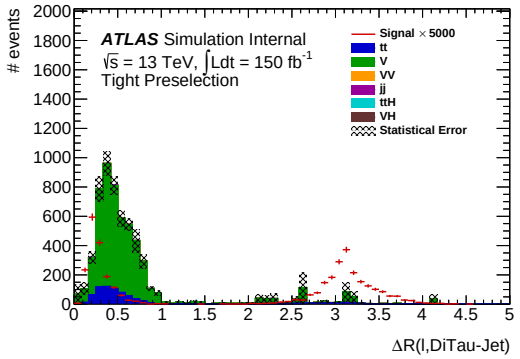

Figure B.12.: Comparison of the signal and background distribution of $\Delta R\,(\text{Di-Tau jet}, \ell)$ after tight preselection.

Bibliography

[1] J. J. Thomson, *Cathode Rays*, The Electrician **39**, 104 (1897)

[2] J. J. Thomson, *Cathode Rays*, Philosophical Magazine **5. 44(293)** (1897)

[3] S. L. Glashow, *Partial Symmetries of Weak Interactions*, Nucl. Phys. **22**, 579 (1961)

[4] A. Salam, *Weak and Electromagnetic Interactions*, Conf. Proc. **C680519**, 367 (1968)

[5] S. Weinberg, *A Model of Leptons*, Phys. Rev. Lett. **19**, 1264 (1967)

[6] M. Gell-Mann, *A Schematic Model of Baryons and Mesons*, Phys. Lett. **8**, 214 (1964)

[7] H. Fritzsch, M. Gell-Mann, H. Leutwyler, *Advantages of the Color Octet Gluon Picture*, Phys. Lett. **47B**, 365 (1973)

[8] D. J. Gross, F. Wilczek, *Ultraviolet Behavior of Nonabelian Gauge Theories*, Phys. Rev. Lett. **30**, 1343 (1973)

[9] H. D. Politzer, *Reliable Perturbative Results for Strong Interactions?*, Phys. Rev. Lett. **30**, 1346 (1973)

[10] A. Petermann, *La normalisation des constantes dans la théorie des quanta. Normalization of constants in the quanta theory*, Helv. Phys. Acta **26**, 499 (1953)

[11] M. Gell-Mann, F. E. Low, *Quantum electrodynamics at small distances*, Phys. Rev. **95**, 1300 (1954)

[12] C. G. Callan, Jr., *Broken scale invariance in scalar field theory*, Phys. Rev. **D2**, 1541 (1970)

[13] K. Symanzik, *Small distance behavior in field theory and power counting*, Commun. Math. Phys. **18**, 227 (1970)

[14] W. Venus, *A LEP summary*, PoS **hep2001**, 284 (2001)

[15] T. R. Junk, A. Juste, *Review of Physics Results from the Tevatron: Higgs Boson Physics*, Int. J. Mod. Phys. **A30(06)**, 1541006 (2015)

[16] C. E. Gerber, C. Vellidis, *Review of Physics Results from the Tevatron: Top Quark Physics*, Int. J. Mod. Phys. A **A30(06)**, 1541005 (2015)

[17] F. Englert, R. Brout, *Broken Symmetry and the Mass of Gauge Vector Mesons*, Phys. Rev. Lett. **13**, 321 (1964)

[18] P. W. Higgs, *Broken Symmetries and the Masses of Gauge Bosons*, Phys. Rev. Lett. **13**, 508 (1964)

[19] G. S. Guralnik, C. R. Hagen, T. W. B. Kibble, *Global Conservation Laws and Massless Particles*, Phys. Rev. Lett. **13**, 585 (1964)

[20] Atlas Collaboration, *Observation of a new particle in the search for the Standard Model Higgs boson with the Atlas detector at the Lhc*, Phys. Lett. **B716**, 1 (2012)

[21] Cms Collaboration, *Observation of a new boson at a mass of 125 GeV with the CMS experiment at the LHC*, Phys. Lett. **B716**, 30 (2012)

[22] Atlas Collaboration, *Search for pair production of Higgs bosons in the $b\bar{b}b\bar{b}$ final state using proton-proton collisions at $\sqrt{s} = 13$ TeV with the ATLAS detector* (2018), arXiv:1804.06174

[23] ATLAS Collaboration, *A search for resonant and non-resonant Higgs boson pair production in the $bb\tau^+\tau^-$ decay channel in pp collisions at $\sqrt{s} = 13$ TeV with the ATLAS detector*, Submitted to: Phys. Rev. Lett. (2018)

[24] ATLAS Collaboration, *Search for Higgs boson pair production in the $\gamma\gamma b\bar{b}$ final state with 13 TeV pp collision data collected by the ATLAS experiment*, Submitted to: JHEP (2018)

[25] ATLAS Collaboration, *Search for Higgs boson pair production in the $\gamma\gamma WW^*$ channel using pp collision data recorded at $\sqrt{s} = 13$ TeV with the ATLAS detector*, Submitted to: Eur. Phys. J. (2018)

[26] Particle Data Group, *Review of Particle Physics*, Chin. Phys. **C40(10)**, 100001 (2016)

[27] G. Arnison, et al. (UA1), *Experimental Observation of Isolated Large Transverse Energy Electrons with Associated Missing Energy at $\sqrt{s} = 540$ GeV*, Phys. Lett. B **122**, 103 (1983)

[28] G. Arnison, et al. (UA1), *Experimental Observation of Lepton Pairs of Invariant Mass Around 95-GeV/c^2 at the CERN SPS Collider*, Phys. Lett. B **126**, 398 (1983)

[29] M. Thomson, *Modern particle physics*, Cambridge University Press, New York (2013)

[30] A. Djouadi, *The Anatomy of electro-weak symmetry breaking. I: The Higgs boson in the standard model*, Phys. Rept. **457**, 1 (2008)

[31] Atlas, Cms Collaborations, *Combined Measurement of the Higgs Boson Mass in pp Collisions at $\sqrt{s} = 7$ and 8 TeV with the ATLAS and CMS Experiments*, Phys. Rev. Lett. **114**, 191803 (2015)

[32] LHC Higgs Cross Section Working Group, *Handbook of LHC Higgs Cross Sections: 4. Deciphering the Nature of the Higgs Sector* (2016), arXiv:1610.07922

[33] A. D. Sakharov, *Violation of CP invariance, C asymmetry, and baryon asymmetry of the universe*, Soviet Physics Uspekhi **34(5)**, 392 (1991)

[34] V. C. Rubin, N. Thonnard, W. K. Ford, Jr., *Rotational properties of 21 SC galaxies with a large range of luminosities and radii, from NGC 4605 /R = 4kpc/ to UGC 2885 /R = 122 kpc/*, Astrophys. J. **238**, 471 (1980)

[35] A. G. Riess, et al., *Observational Evidence from Supernovae for an Accelerating Universe and a Cosmological Constant*, The Astronomical Journal **116(3)**, 1009 (1998)

[36] M. J. G. Veltman, *The Infrared - Ultraviolet Connection*, Acta Phys. Polon. **B12**, 437 (1981)

[37] I. Brock, T. Schörner-Sadenius, editors, *Physics at the Terascale*, Springer Verlag, Berlin; Heidelberg; New York (2006)

[38] G. R. Farrar, P. Fayet, *Phenomenology of the Production, Decay, and Detection of New Hadronic States Associated with Supersymmetry*, Phys. Lett. **76B**, 575 (1978)

[39] P. Fayet, *Supergauge Invariant Extension of the Higgs Mechanism and a Model for the electron and Its Neutrino*, Nucl. Phys. **B90**, 104 (1975)

[40] P. Fayet, *Supersymmetry and Weak, Electromagnetic and Strong Interactions*, Phys. Lett. **64B**, 159 (1976)

[41] P. Fayet, *Spontaneously Broken Supersymmetric Theories of Weak, Electromagnetic and Strong Interactions*, Phys. Lett. **69B**, 489 (1977)

[42] P. Fayet, *Relations Between the Masses of the Superpartners of Leptons and Quarks, the Goldstino Couplings and the Neutral Currents*, Phys. Lett. **84B**, 416 (1979)

[43] K. Inoue, et al., *Aspects of Grand Unified Models with Softly Broken Supersymmetry*, Prog. Theor. Phys. **68**, 927 (1982), [Erratum: Prog. Theor. Phys.70,330(1983)]

[44] J. E. Kim, *Light Pseudoscalars, Particle Physics and Cosmology*, Phys. Rept. **150**, 1 (1987)

[45] M. Trodden, *Electroweak baryogenesis: A Brief review*, in *Proceedings, 33rd Rencontres de Moriond 98 electrowek interactions and unified theories: Les Arcs, France, Mar 14-21, 1998* (1998)

[46] H. Georgi, *A Model of Soft CP Violation*, Hadronic J. **1**, 155 (1978)

[47] J. F. Gunion, et al., *The Higgs Hunter's Guide*, Front. Phys. **80**, 1 (2000)

[48] G. C. Branco, et al., *Theory and phenomenology of two-Higgs-doublet models*, Phys. Rept. **516**, 1 (2012)

[49] H. E. Haber, G. L. Kane, T. Sterling, *The Fermion Mass Scale and Possible Effects of Higgs Bosons on Experimental Observables*, Nucl. Phys. **B161**, 493 (1979)

[50] L. J. Hall, M. B. Wise, *Flavor changing Higgs-boson couplings*, Nucl. Phys. **B187**, 397 (1981)

[51] J. F. Donoghue, L. F. Li, *Properties of Charged Higgs Bosons*, Phys. Rev. **D19**, 945 (1979)

[52] R. Barnett, et al., *Implications of a light Higgs scalar*, Physics Letters B **136(3)**, 191 (1984)

[53] R. M. Barnett, G. Senjanovic, D. Wyler, *Tracking Down Higgs Scalars With Enhanced Couplings*, Phys. Rev. **D30**, 1529 (1984)

[54] M. Jacob, editor, *ECFA-CERN Workshop on large hadron collider in the LEP tunnel, Lausanne and CERN, Geneva, Switzerland, 21-27 Mar 1984: Proceedings. 1.* (1984)

[55] L. Evans, P. Bryant, *LHC Machine*, JINST **3**, S08001 (2008)

[56] ATLAS Collaboration, *Luminosity determination in pp collisions at $\sqrt{s}$ = 8 TeV using the ATLAS detector at the LHC*, Eur. Phys. J. **C76(12)**, 653 (2016)

[57] ATLAS Collaboration, *The ATLAS Experiment at the CERN Large Hadron Collider*, JINST **3**, S08003 (2008)

[58] CMS Collaboration, *The CMS Experiment at the CERN LHC*, JINST **3**, S08004 (2008)

[59] A. A. Alves, Jr., et al. (LHCb), *The LHCb Detector at the LHC*, JINST **3**, S08005 (2008)

[60] K. Aamodt, et al. (ALICE), *The ALICE experiment at the CERN LHC*, JINST **3**, S08002 (2008)

[61] ATLAS Collaboration, *ATLAS Insertable B-Layer Technical Design Report* (2010)

[62] ATLAS Collaboration, *ATLAS Transition Radiation Tracker (TRT): Straw Tube Gaseous Detectors at High Rates*, Technical Report ATL-INDET-PROC-2013-005, CERN, Geneva (2013)

[63] ATLAS Collaboration, *Technical Design Report for the Phase-I Upgrade of the ATLAS TDAQ System*, Technical Report CERN-LHCC-2013-018. ATLAS-TDR-023 (2013)

[64] S. Höche, *Introduction to parton-shower event generators*, in *Proceedings, Theoretical Advanced Study Institute in Elementary Particle Physics: Journeys Through the Precision Frontier: Amplitudes for Colliders (TASI 2014): Boulder, Colorado, June 2-27, 2014*, pages 235–295 (2015)

[65] A. Buckley, et al., *General-purpose event generators for LHC physics*, Phys. Rept. **504**, 145 (2011)

[66] ATLAS Collaboration, *The ATLAS Simulation Infrastructure*, Eur. Phys. J. **C70** (2010)

[67] S. Agostinelli, et al. (GEANT4), *GEANT4: A Simulation toolkit*, Nucl. Instrum. Meth. **A506**, 250 (2003)

[68] ATLAS Collaboration, *Performance of the Fast ATLAS Tracking Simulation (FATRAS) and the ATLAS Fast Calorimeter Simulation (FastCaloSim) with single particles*, Technical Report ATL-SOFT-PUB-2014-001, CERN, Geneva (2014)

[69] ATLAS Collaboration, *The simulation principle and performance of the ATLAS fast calorimeter simulation FastCaloSim*, Technical Report ATL-PHYS-PUB-2010-013, CERN, Geneva

[70] ATLAS Collaboration, *The simulation principle and performance of the ATLAS fast calorimeter simulation FastCaloSim*, Technical Report ATL-PHYS-PUB-2010-013, CERN, Geneva (2010)

[71] G. C. Blazey, et al., *Run II jet physics*, in *QCD and weak boson physics in Run II. Proceedings, Batavia, USA, March 4-6, June 3-4, November 4-6, 1999* (2000)

[72] S. Catani, et al., *Longitudinally invariant K_t clustering algorithms for hadron hadron collisions*, Nucl. Phys. **B406**, 187 (1993)

[73] S. D. Ellis, D. E. Soper, *Successive combination jet algorithm for hadron collisions*, Phys. Rev. **D48** (1993)

[74] Y. L. Dokshitzer, et al., *Better jet clustering algorithms*, JHEP **08** (1997)

[75] M. Cacciari, G. P. Salam, G. Soyez, *The Anti-k(t) jet clustering algorithm*, JHEP **04**, 063 (2008)

[76] J. Thaler, K. Van Tilburg, *Identifying Boosted Objects with N-subjettiness*, JHEP **03**, 015 (2011)

[77] A. J. Larkoski, G. P. Salam, J. Thaler, *Energy Correlation Functions for Jet Substructure*, JHEP **06**, 108 (2013)

[78] A. J. Larkoski, I. Moult, D. Neill, *Power Counting to Better Jet Observables*, JHEP **12**, 009 (2014)

[79] A. J. Larkoski, I. Moult, D. Neill, *Analytic Boosted Boson Discrimination*, JHEP **05**, 117 (2016), 1507.03018

[80] D. Kirchmeier, A. Straessner, M. Kobel, *Reconstruction and Identification of Boosted Tau Pair Topologies at ATLAS*, Master's thesis (2015)

[81] K. Abeling, *Search for di-Higgs production in the $\gamma\gamma WW^*$ decay channel with the 1-lepton final state and the boosted topology at* ATLAS, Master's thesis, II. Physikalisches Institut, Georg-August-Universität Göttingen (2017), II.Physik-UniGö-MSc-2017/08

[82] J. Thaler, K. Van Tilburg, *Maximizing Boosted Top Identification by Minimizing N-subjettiness*, JHEP **02**, 093 (2012)

[83] J. Alwall, et al., *The automated computation of tree-level and next-to-leading order differential cross sections, and their matching to parton shower simulations*, JHEP **07**, 079 (2014)

[84] T. Sjostrand, S. Mrenna, P. Z. Skands, *A Brief Introduction to PYTHIA 8.1*, Comput. Phys. Commun. **178**, 852 (2008)

[85] R. D. Ball, et al., *Parton distributions with LHC data*, Nucl. Phys. **B867**, 244 (2013)

[86] ATLAS Collaboration, *ATLAS Run 1 Pythia8 tunes*, Technical Report ATL-PHYS-PUB-2014-021, CERN, Geneva (2014)

[87] B. Hespel, D. Lopez-Val, E. Vryonidou, *Higgs pair production via gluon fusion in the Two-Higgs-Doublet Model*, JHEP **09**, 124 (2014)

[88] M. Bahr, et al., *Herwig++ Physics and Manual*, Eur. Phys. J. **C58**, 639 (2008)

[89] H.-L. Lai, et al., *New parton distributions for collider physics*, Phys. Rev. **D82**, 074024 (2010)

[90] P. M. Nadolsky, et al., *Implications of CTEQ global analysis for collider observables*, Phys. Rev. **D78**, 013004 (2008)

[91] M. H. Seymour, A. Siodmok, *Constraining MPI models using σ_{eff} and recent Tevatron and LHC Underlying Event data*, JHEP **10**, 113 (2013)

[92] ATLAS Collaboration, *Identification and energy calibration of hadronically decaying tau leptons with the ATLAS experiment in pp collisions at $\sqrt{s}$=8 TeV*, Eur. Phys. J. **C75(7)** (2015)

[93] R. Brun, F. Rademakers, *ROOT: An object oriented data analysis framework*, Nucl. Instrum. Meth. **A389**, 81 (1997)

[94] K. Cranmer, et al. (ROOT), *HistFactory: A tool for creating statistical models for use with RooFit and RooStats*, CERN-OPEN-2012-016 (2012)

[95] S. Alioli, et al., *A general framework for implementing NLO calculations in shower Monte Carlo programs: the POWHEG BOX*, JHEP **06**, 043 (2010)

[96] ATLAS Collaboration, *Example ATLAS tunes of Pythia8, Pythia6 and Powheg to an observable sensitive to Z boson transverse momentum*, Technical Report ATL-PHYS-PUB-2013-017, CERN, Geneva (2013)

[97] ATLAS Collaboration, *Search for pair production of Higgs bosons in the $b\bar{b}b\bar{b}$ final state using proton−proton collisions at $\sqrt{s} = 13$ TeV with the ATLAS detector*, ATLAS-CONF-2016-049 (2016)

[98] ATLAS Collaboration, *Electron efficiency measurements with the ATLAS detector using 2012 LHC proton–proton collision data*, Eur. Phys. J. **C77(3)** (2017)

[99] ATLAS Collaboration, *Muon reconstruction performance of the ATLAS detector in proton–proton collision data at $\sqrt{s}$ =13 TeV*, Eur. Phys. J. **C76(5)** (2016)

[100] ATLAS Collaboration, *Monte Carlo Calibration and Combination of In-situ Measurements of Jet Energy Scale, Jet Energy Resolution and Jet Mass in ATLAS*, ATLAS-CONF-2015-037 (2015)

[101] ATLAS Collaboration, *Jet Calibration and Systematic Uncertainties for Jets Reconstructed in the ATLAS Detector at $\sqrt{s} = 13$ TeV*, Technical Report ATL-PHYS-PUB-2015-015, CERN, Geneva (2015)

[102] C. Wiel, *Reconstruction and Identification of Boosted Tau Pairs in the Semi-Leptonic Decay Channel at ATLAS*, Master's thesis, TU Dresden (2018)

[103] G. Cowan, K. Cranmer, E. Gross, O. Vitells, *Asymptotic formulae for likelihood-based tests of new physics*, Eur. Phys. J. **C71**, 1554 (2011), [Erratum: Eur. Phys. J.C73,2501(2013)]

[104] A. L. Read, *Presentation of search results: The CL(s) technique*, J. Phys. **G28**, 2693 (2002)

Danksagung

Danke an Stan und Jason für die Betreuung und die Möglichkeit, meine Masterarbeit in der Gruppe zu schreiben, und an die ganze Arbeitsgruppe, in der ich mich während des letzten Jahres sehr wohl und willkommen gefühlt habe. Danke an Petar für die Beantwortung von allen möglichen Fragen und guten Unterhaltungen, und ein ganz großes und besonderes Danke an Kira - du warst Hilfe in allen Forschungslagen, und ohne dich wäre ich in dem Jahr sicher nicht so weit gekommen! #worksoutofthebox
Danke auch an Arnaud aus Uppsala und an Pawel und Anna aus Krakau für die Möglichkeit, Forschungsaufenthalte bei ihnen in wunderbaren Städten zu verbringen und meine Arbeit mit ihnen diskutieren zu können.

Ein ganz großes Danke geht natürlich an meine Familie - meine Eltern und meinen Bruder. Ihr habt mich immer bedingungslos unterstützt in meinem Studium, auch wenn das sicherlich auch für euch nicht immer leicht war. Danke für die Sicherheit, die ihr mir damit geboten habt, und Danke für eine Tür, die immer in beide Richtungen offen ist. Danke natürlich auch an meine Großeltern, sowohl nach Geismar als auch nach Herne.

Danke an all die anderen Menschen, die mich auf meinem bisherigen Weg begleitet haben – Leonie und Linda, dass ich mit euch über alles reden kann und ihr egal was passiert ist, für mich da wart, Bene, für Kartenspiele, entspannen, die besten Musiktipps und allgemein coole Erinnerungen, den Menschen vom Forum, dass sie mich im dritten Semester in ihre Gruppe aufgenommen haben und mein Studium und Sozialleben gerettet haben, den RTL+N Jungs für einfach nur geile Abende zum Abschalten und Ablenken, und Hannah für witzige Tanzstunden.

Danke an Finja für tanzvolle Stunden und interessante Diskussionen in stressigen Tagen und Wochen. Ich bin sehr froh, dich getroffen zu haben, und es macht wunderbar viel Spaß, mit dir zu sein! Danke für anregenden Gedankenaustausch, konstruktive Problemlösungsansätze und gemeinsames verkopft sein ;) #küchentisch

Zu guter Letzt Danke an Stephan und das evangelische Studienwerk - du hast mich durch eine für mich schwere Zeit wunderbar begleitet, und ich bin dankbar für die Offenheit und Unterstützung, die ich von dir bekommen habe!

#worksoutofthebox – Maschin

Erklärung nach §17(9) der Prüfungsordnung für den Bachelor-Studiengang Physik und den Master-Studiengang Physik an der Universität Göttingen:

Hiermit erkläre ich, dass ich diese Abschlussarbeit selbständig verfasst habe, keine anderen als die angegebenen Quellen und Hilfsmittel benutzt habe und alle Stellen, die wörtlich oder sinngemäß aus veröffentlichten Schriften entnommen wurden, als solche kenntlich gemacht habe.
Darüberhinaus erkläre ich, dass diese Abschlussarbeit nicht, auch nicht auszugsweise, im Rahmen einer nichtbestandenen Prüfung an dieser oder einer anderen Hochschule eingereicht wurde.

Göttingen, den 8. April 2019

(Nils Gillwald)